Supporting Information

A tetraphenyl-*p*-phenylenediamine- and benzodithiophene-4,8-dione-based conjugated microporous polymer as a robust cathode for durable aqueous Zn batteries

Jiahe Zhan,[a] Sung-En Lin,[b,c] Ijaz Ali,[a] Bo-Chun Chen,[b,c] Trakarn Yimtrakarn,[b,c] Pilgun Oh,[d,e] Rong Ho Lee,[f] Watchareeya Kaveevivitchai,*[b,c,g] and Ahmed F. M. EL-Mahdy*[a]

[a] Department of Materials and Optoelectronic Science, National Sun Yat-Sen University, Kaohsiung 80424, Taiwan

[b] Department of Chemical Engineering, National Cheng Kung University, Tainan City 70101, Taiwan

[c] Hierarchical Green-Energy Materials (Hi-GEM) Research Center, National Cheng Kung University, Tainan City 70101, Taiwan

[d] Department of Smart Green Technology Engineering, Pukyong National University, Busan 48547, Republic of Korea

[e] Department of Nanotechnology Engineering, Pukyong National University, Busan 48547, Republic of Korea

[f] Department of Chemical Engineering, National Chung Hsing University, Taichung, 402, Taiwan

[g] Academy of Innovative Semiconductor and Sustainable Manufacturing, National Cheng Kung University, Tainan City 70101, Taiwan

Corresponding authors:

Ahmed F. M. EL-Mahdy,

E-mail: ahmedelmahdy@mail.nsysu.edu.tw

Watchareeya Kaveevivitchai

Email: wkaveechai@mail.ncku.edu.tw

S1. Materials

N^{1},*N*^{1},*N*^{4},*N*^{4}-tetraphenyl-*p*-phenylenediamine, *N*,*N*-Dimethylthiophene-3-carboxamide, dimethylformamide (DMF), and 1,4-dioxane were purchased from Sigma-Aldrich. N-Bromosuccinimide (NBS) and tetrakis(triphenylphosphine)palladium(0) [$Pd(PPh_3)_4$] were obtained from Acros. 1,4-phenyldiboronic acid was purchased from TCI. Potassium carbonate (K_2CO_3) was purchased from Combi-Blocks. n-Butyllithium (n-BuLi, 2.5 M in hexane) was obtained from Albemarle. Unless otherwise stated, all reagents were used as received, and anhydrous solvents were used for moisture-sensitive reactions.

S2. Characterization

Fourier transform infrared (FTIR) spectra were recorded on a Bruker Tensor 27 spectrophotometer using the standard KBr pellet method. Each spectrum was collected with 32 scans at a resolution of 4 cm^{-1}. Solid-state nuclear magnetic resonance (SSNMR) experiments were performed on a Bruker Avance 400 MHz spectrometer equipped with a magic-angle spinning (MAS) probe; 32,000 scans were accumulated to obtain a high signal-to-noise ratio. TPDA-4Br was dissolved in HPLC-grade methanol (or acetonitrile) to prepare a ~10–50 μM solution, filtered through a 0.22 μm PTFE syringe filter, and then analyzed by ESI-MS using a Thermo Fisher Orbitrap Exploris 120 mass spectrometer at the NSYSU KHVIC facility. Thermal stability was evaluated by thermogravimetric analysis (TGA) using a TA Q-50 analyzer. Samples were placed in platinum crucibles and heated from 40 to 700 °C at 20 °C min^{-1} under a continuous nitrogen flow of 50 mL min^{-1}. Porosity and textural properties were determined from N_2 adsorption–desorption isotherms were recorded on a BelSorp Max instrument. Before analysis, ~50 mg of each sample was Soxhlet-extracted with anhydrous tetrahydrofuran for 24 h, filtered, and degassed under vacuum at 150 °C for

10 h. Gas adsorption measurements were carried out at 77 K over a relative pressure (P/P_0) range of 0.01–0.99. Specific surface areas were calculated using the Brunauer–Emmett–Teller (BET) method, and pore-size distributions were derived from quenched solid density functional theory (QSDFT) analysis. Morphologies were examined by field-emission scanning electron microscopy (FE-SEM) on a JEOL JSM-7610F. Before imaging, samples were sputter-coated with Pt for 100 s to improve conductivity. Transmission electron microscopy (TEM) was carried out on a JEOL JEM-2100 microscope operated at 200 kV to probe the internal microstructure.

Ex-situ FTIR data were recorded on Nicolet iS5 or Nicolet 6700, Thermo Scientific. *Ex-situ* XPS measurements were performed on ULVAC PHI 5000 VersaProbe III with Al Kα (1487 eV) as an X-ray source. Survey scans were collected with a pass energy of 100 eV, followed by high-resolution scans of the C 1s, N 1s, O 1s and Zn 2p regions with a pass energy of 20 eV. All spectra were charge-corrected relative to the C 1s component at 284.5 eV binding energy and analyzed using CasaXPS software. *Ex-situ* ^{1}H solid-state nuclear magnetic resonance (NMR) spectra were recorded on a Bruker Avance III HD 400MHz NMR. *Ex-situ* scanning electron microscopy (SEM) images were collected on a SU8010 HR-FESEM scanning electron microscope. *Ex-situ* powder X-ray diffraction (PXRD) patterns were collected on Bruker D8 Advance ECO. The pH variation during discharge/charge processes was measured using a Suntex SP-2100 pH meter. 2-electrode cell configuration containing 5 mL of 1 M $ZnSO_4$ electrolyte was used with pH probe in the cells to directly monitor the pH values in real time. Elemental analysis (Zn and S) was performed by inductively coupled plasma-optical emission spectroscopy (ICP-OES) using Thermo Scientific iCAP™ 7400.

S3. Synthetic Procedures of Monomers

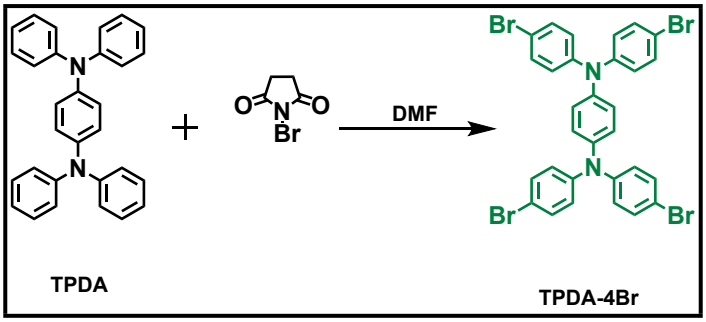

Scheme S1. Synthesis of TPDA-4Br.

***N*^{1},*N*^{1},*N*^{4},*N*^{4}-Ttetrakis(4-bromophenyl)-*p*-phenylenediamine (TPDA-4Br).** Bromination of *N*^{1},*N*^{1},*N*^{4},*N*^{4}-tetraphenyl-*p*-phenylenediamine (TPDA) was performed as reported previously [S1]. Briefly, in an ice bath, the TPPDA (2.42 mmol, 1 g) and dry DMF (40 mL) were charged together into a 50 mL flask. Secondly, a solution of (*N*-Bromosuccinimide) NBS (10.8 mmol, 1.94 g) dissolved in 20 mL of dry DMF was added wisely to the prime solution under icy conditions and gentle stirring for 30 min. After that, the mixture was left overnight under magnetic stirring at ambient conditions. Finally, flask contents were poured onto ice water, filtered, washed several times as well using ethanol till obtaining a white powder (1.64 g, 93% yield). FTIR: 1576, 1499, 1016 cm^{-1} (Figure S1). The ^{1}H-NMR ($CDCl_3$, 25 °C, 600 MHz): 7.35 (d, 8H), 6.94 (m, 12H). ^{13}C NMR ($CDCl_3$, 25 °C, 500 MHz): 132.3, 125.5, 125.2 ppm. *HRMS* (*ESI*): *m/z* calculated for $C_{30}H_{20}Br_4N_2$: 728.1; found 728.69 (Figure S2).

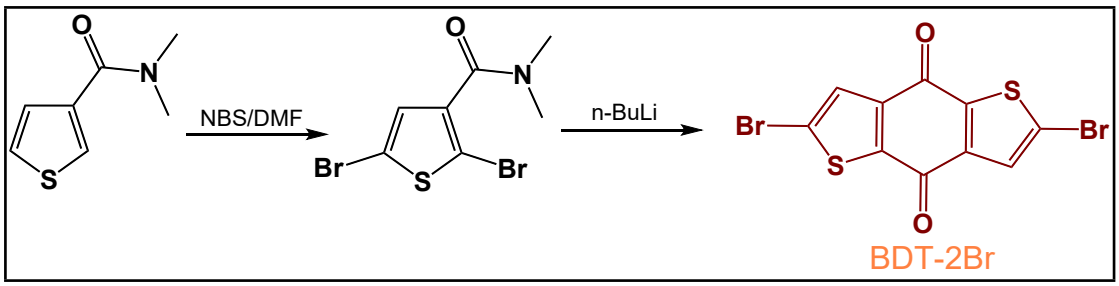

Scheme S2. Synthesis of BDT-2Br.

Synthesis of 2,5-dibromo-*N*,*N*-dimethylthiophene-3-carboxamide: A solution of N,N-dimethylthiophene-3-carboxamide (3.0 g, 19.3 mmol) in anhydrous DMF (50 mL) was prepared, and a solution of N-bromosuccinimide (NBS; 8.6 g, 48.25 mmol) in anhydrous DMF (20 mL) was added dropwise under continuous stirring. The reaction mixture was stirred at room temperature for 4 h. After completion, the mixture was poured into water (600 mL) and extracted with ethyl acetate. The combined organic layers were dried, filtered, and concentrated under reduced pressure. The crude product was purified by silica gel column chromatography (hexane/ethyl acetate = 6:1, v/v) to afford 2,5-dibromo-N,N-dimethylthiophene-3-carboxamide as a yellow oil (5.4 g, 90% yield).

Synthesis of 2,6-dibromobenzo[1,2-b:4,5-b']dithiophene-4,8-dione (BDT-2Br): A suspension of 2,5-dibromo-*N,N*-dimethylthiophene-3-carboxamide (2.00 g, 6.4 mmol) in anhydrous THF (50 mL) was cooled to −78 °C under a nitrogen atmosphere. A solution of *n*-butyllithium (2.50 mL, 6.4 mmol, 2.5 M in hexane) was then added dropwise. The reaction mixture was stirred at −70 °C for 4 h and subsequently allowed to warm to room temperature. The reaction was quenched with saturated aqueous NH_4Cl (20 mL), and the resulting precipitate was collected. Purification by silica gel column chromatography ($CHCl_3$ as eluent) afforded BDTh-2Br as an orange solid (1.06 g, 44% yield).

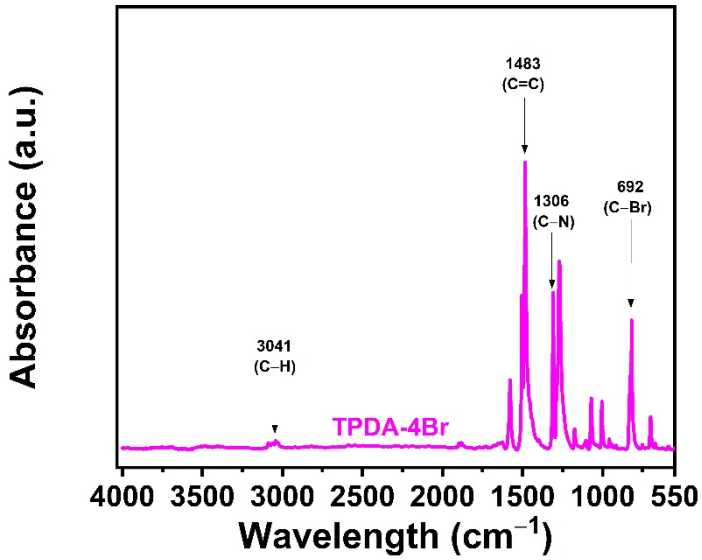

Figure S1. FTIR spectrum of TPDA-4Br.

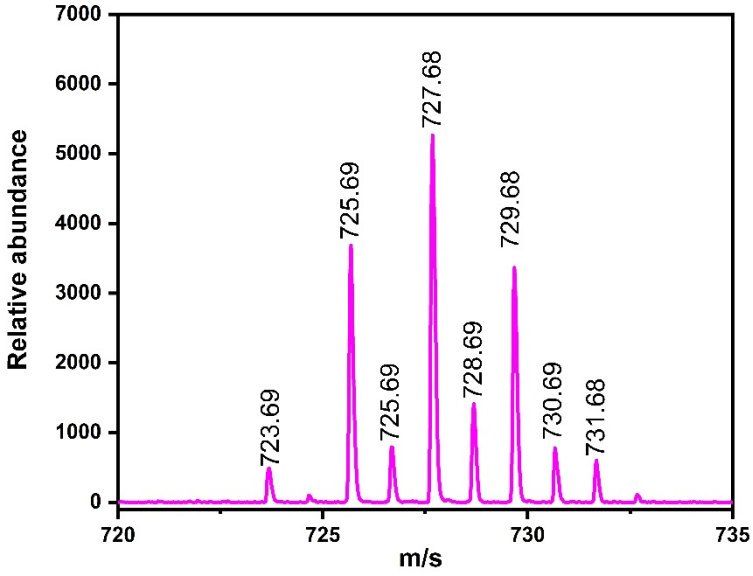

Figure S2. Mass spectrum of TPDA-4Br.

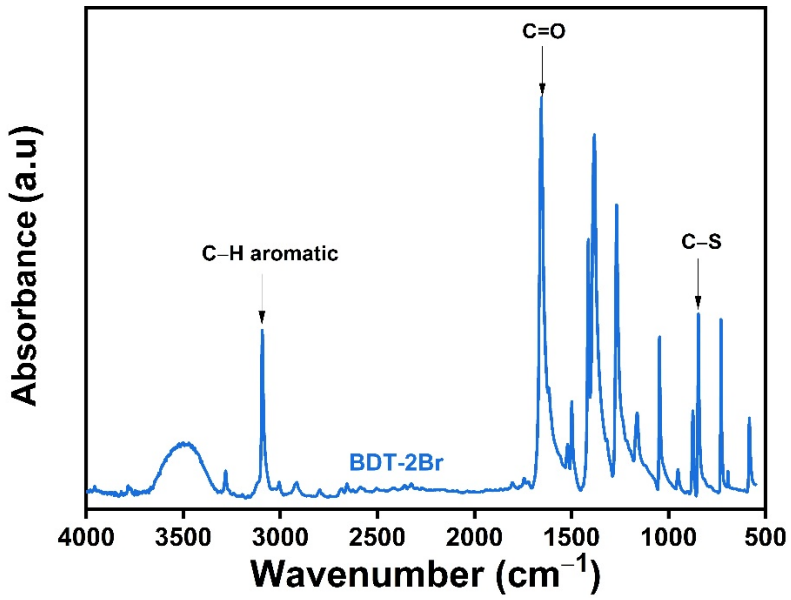

Figure S3. FTIR spectrum of BDT-2Br.

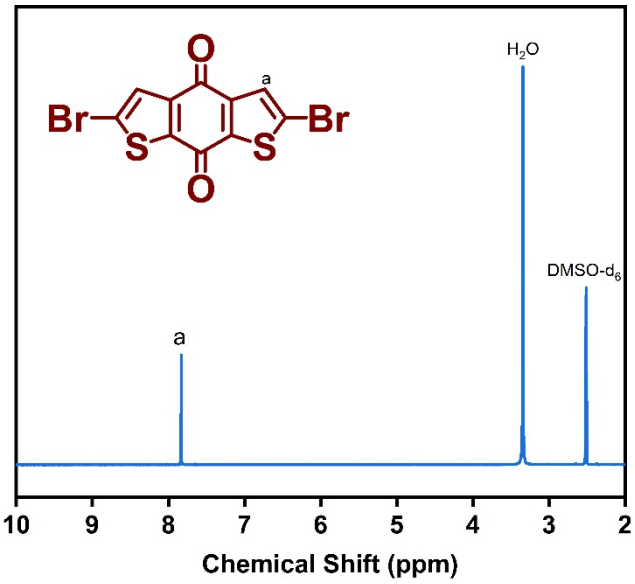

Figure S4. ^{1}H NMR spectrum of BDT-2Br.

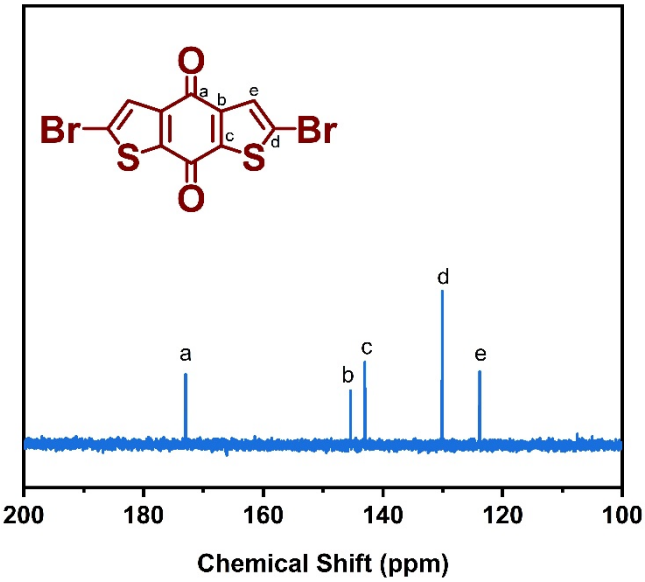

Figure S5. ^{13}C NMR spectrum of BDT-2Br.

S4. Synthetic Procedures of CMPs

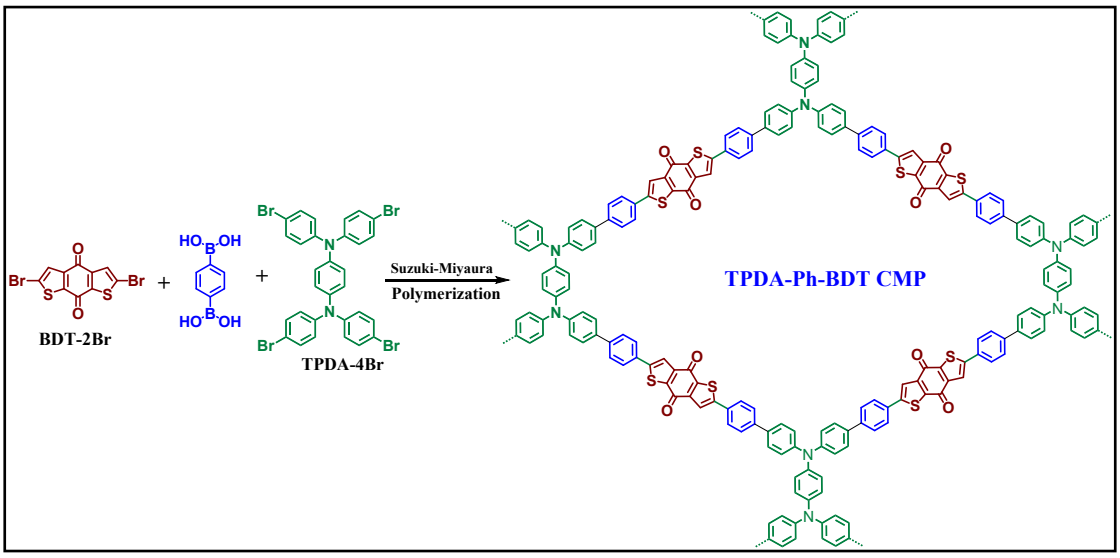

Scheme S3. Synthesis of TPDA-Ph-BDT CMP.

BDT-2Br (155.76 mg, 0.412 mmol), TPDA-4Br (150 mg, 0.21 mmol), $Pd(PPh_3)_4$ (24 mg, 0.02 mmol), and Ph-2BO (139.6 mg, 0.84 mmol) were combined in a 50 mL Pyrex tube and evacuated for 15 min. DMF (25 mL) and an aqueous K_2CO_3 solution (550 mg in 5 mL H_2O, 3.97 mmol) were then added. The tube was flame-sealed and heated at 130 °C for 3 days. After cooling to room temperature, the tube was opened, and the

resulting precipitate was collected by filtration, washed thoroughly with methanol, and vacuum-dried at 120 °C overnight to afford TPDA-Ph-BDT CMP as a brown solid (81% yield).

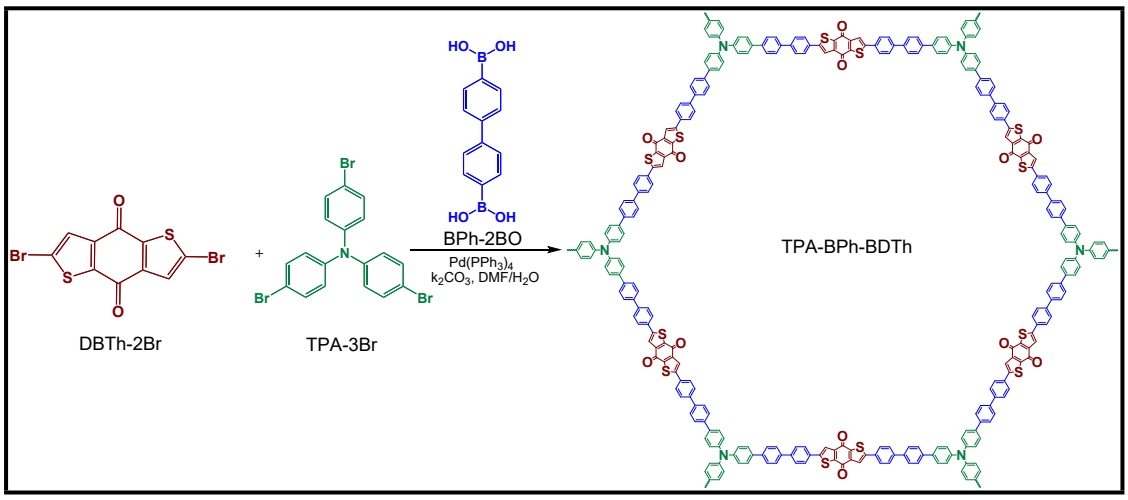

Scheme S4. Synthesis of TPA-BPh-BDTh CMP.

A mixture of tris(4-bromophenyl)amine (TPA-3Br, 200 mg, 0.40 mmol), 2,6-dibromobenzo[1,2-b:4,5-b′]dithiophene-4,8-dione (BDTh-2Br, 235.4 mg, 0.60 mmol), 4,4′-biphenyl diboronic acid (BPh-2BO, 301.0 mg, 1.20 mmol), and tetrakis(triphenylphosphine)palladium(0) [$Pd(PPh_3)_4$, 40 mg, 0.034 mmol] was charged into a 100 mL two-neck round-bottom flask. The flask was degassed by three vacuum–nitrogen cycles. Dry DMF (50 mL) and an aqueous K_2CO_3 solution (1.0 g in 10 mL H_2O) were then added, and the reaction mixture was stirred at 130 °C under nitrogen for 48 h. After cooling to room temperature, the resulting solid was collected by centrifugation and washed sequentially with acetone (3×) and THF (3×) until the supernatant became colorless. The product was dried under vacuum at 100 °C overnight to afford TPA-BPh-BDTh CMP as a brown solid (76% yield).

S5. BET Parameters

Table S1. BET parameters of the synthesized TPDA-Ph-BDT CMP.

CMP	SBET ($m^2\ g^{-1}$)	Pore size (nm)	Pore volume ($cm^3\ g^{-1}$)
TPDA-Ph-BDT	273	1.34~3.41/3.96~6.71	0.43

S6. Thermogravimetric Analysis (TGA) Profile

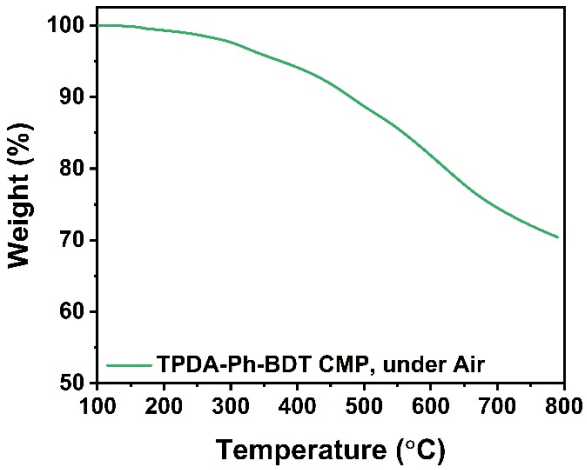

Figure S6. TGA curve of TPDA-Ph-BDT CMP under an air environment.

Table S2. Values of $T_{d10\%}$ and char yield of TPDA-Ph-BDT CMP.

CMP	T_{d10} (°C)	Char yield(%)
TPDA-Ph-BDT, under N_2	673	81.25
TPDA-Ph-BDT, under Air	479	70.39

S7. Elemental mapping (EDS mapping) data

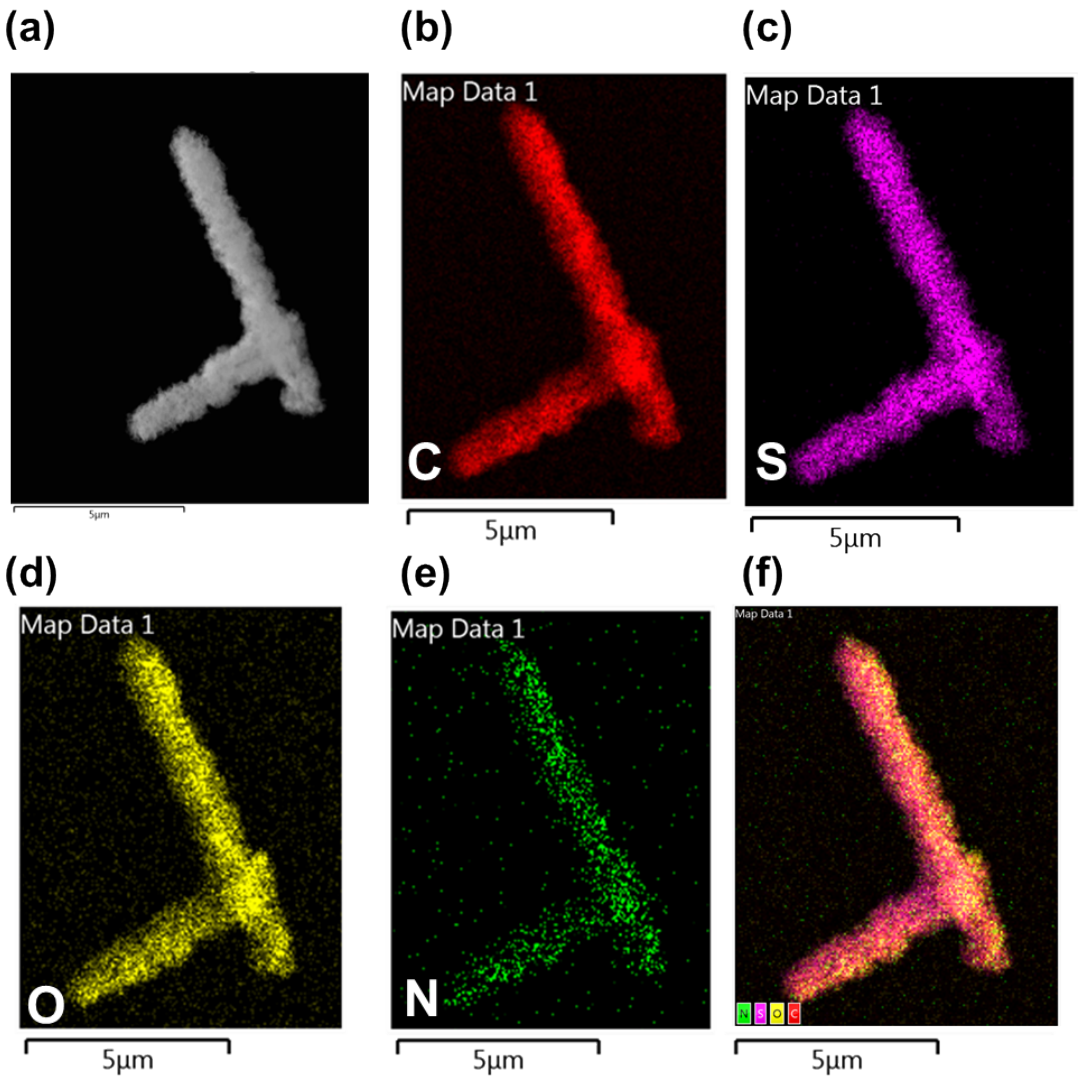

Figure S7. (a) TEM image and (b-f) corresponding EDS elemental mapping images of TPDA-Ph-BDT CMP, showing the distribution of the constituent elements; (b) C, (c) S, (d) O, (e) N, and (f) the overlay map, confirming uniform elemental dispersion across the rod-like particle.

S8. FTIR and BET for TPA-BPH-BDTh.

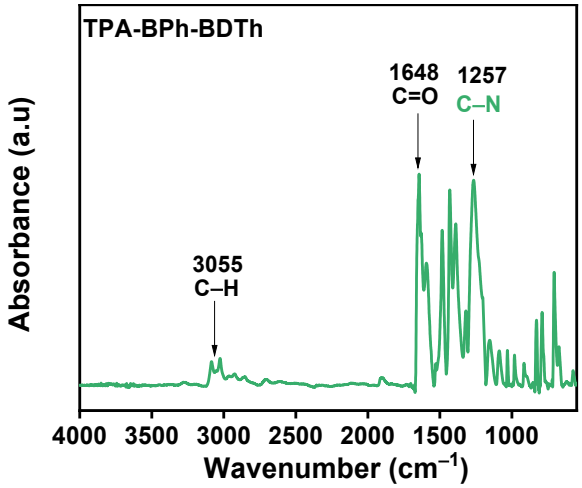

Figure 8. FTIR spectra of the TPA-BPh-BDTh CMP.

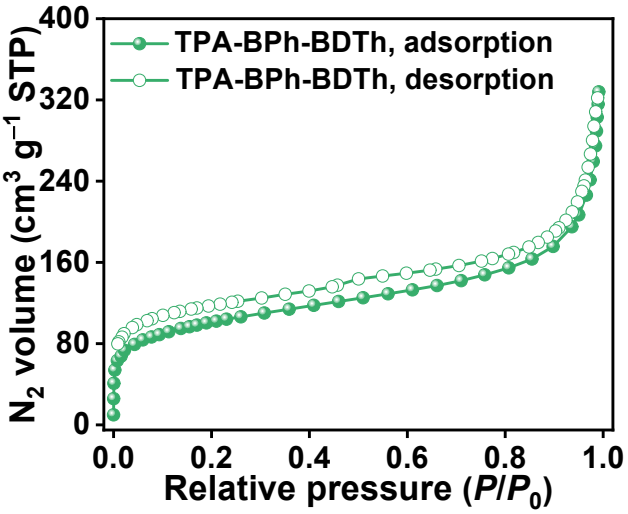

Figure 9. N_2 adsorption–desorption isotherm of the TPA-BPh-BDTh CMP.

S9. Electrochemical properties

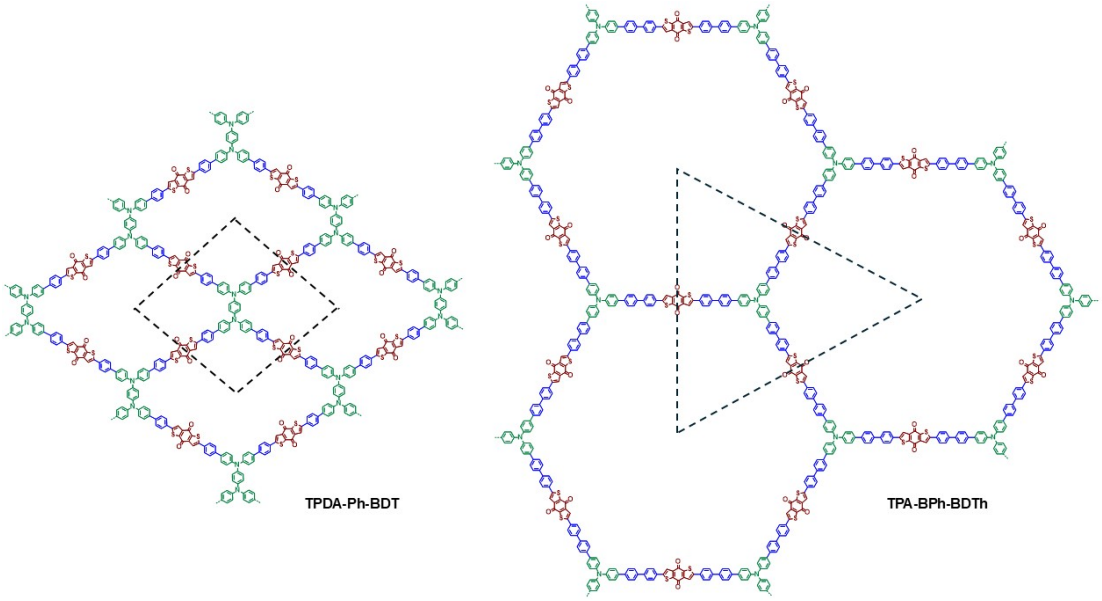

Figure S10. Structure of TPDA-Ph-BDT compared with that of TPA-BPh-BDTh and their repeating units. TPDA-Ph-BDT, which contains four C=O and two N amine active sites per repeating unit, was electrochemically investigated in comparison with TPA-BPh-BDTh, which contains three C=O and one N amine per repeating unit. The two CMPS have the same redox-active BDT unit (shown in brown). The main difference is the amine units (shown in green), i.e., tetrafunctional TPDA unit in the case of TPDA-Ph-BDT leading to a tightly cross-linked network vs. trifunctional TPA unit in the case of TPA-BPh-BDTh, which leads to different connectivity in space.

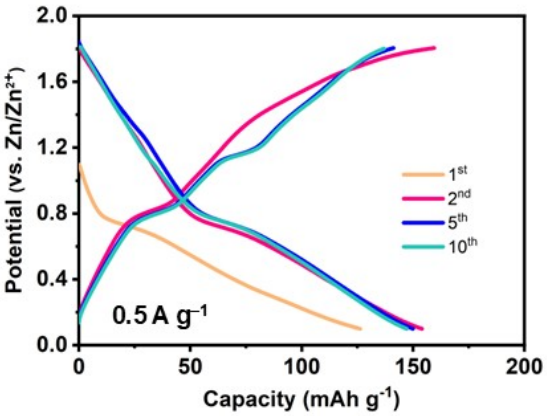

Figure S11. Galvanostatic discharge/charge profiles of TPDA-Ph-BDT CMP at 0.5 A g^{-1}.

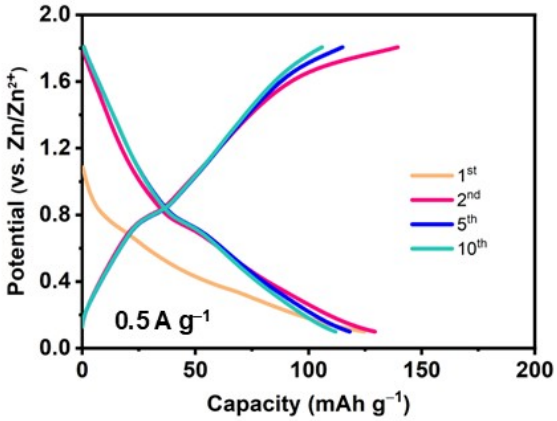

Figure S12. Galvanostatic discharge/charge profiles of TPA-BPh-BDTh at 0.5 A g^{-1}.

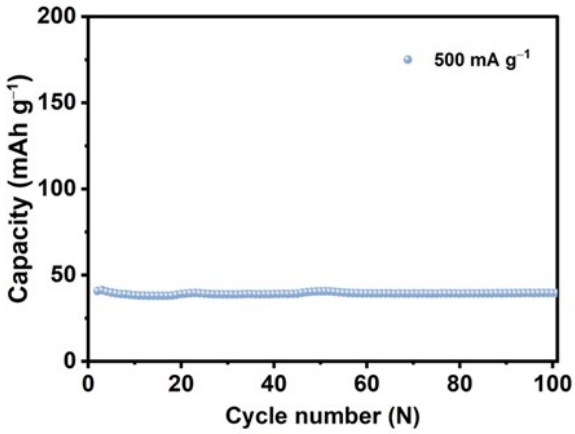

Figure S13. Electrochemical properties of Ketjen black conductive carbon cycled in the voltage range of 0.10–1.85 V (electrode ratio = Ketjen black: PVDF = 9:1).

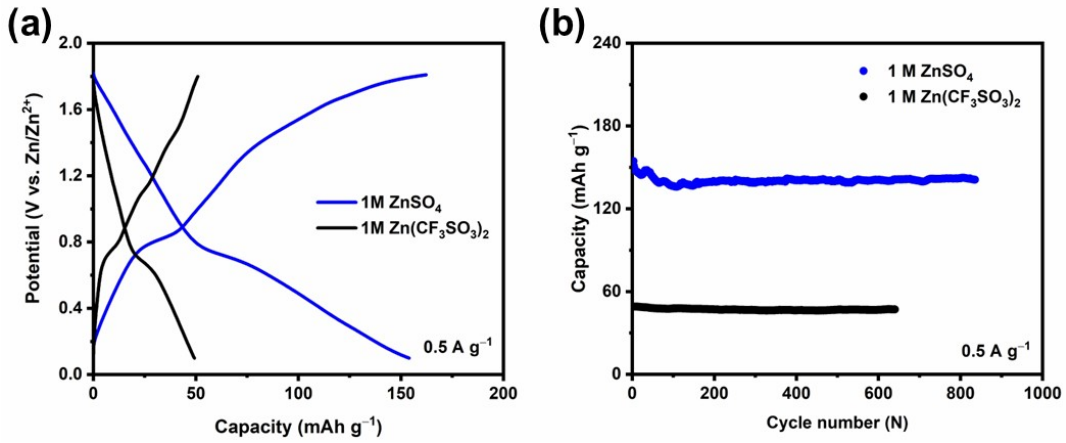

Figure S14. (a) and (b) Voltage profiles and capacity retention plots of TPDA-Ph-BDT in $Zn(CF_3SO_3)_2$ and $ZnSO_4$ aqueous electrolytes at 500 mA g^{-1}.

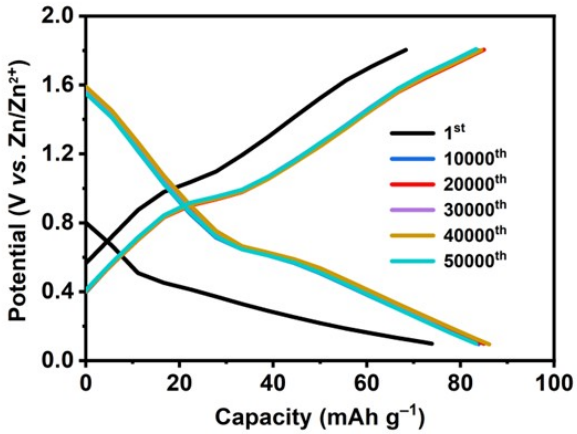

Figure S15. Voltage profiles of TPDA-Ph-BDT CMP at different cycle numbers at a current density of 20 A g^{-1}, revealing high cycling stability of the robust CMP framework.

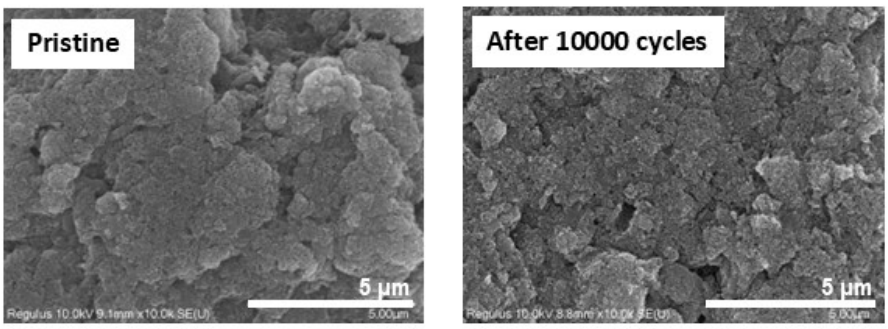

Figure S16. SEM images of TPDA-Ph-BDT electrodes at the pristine state and after 10000 cycles.

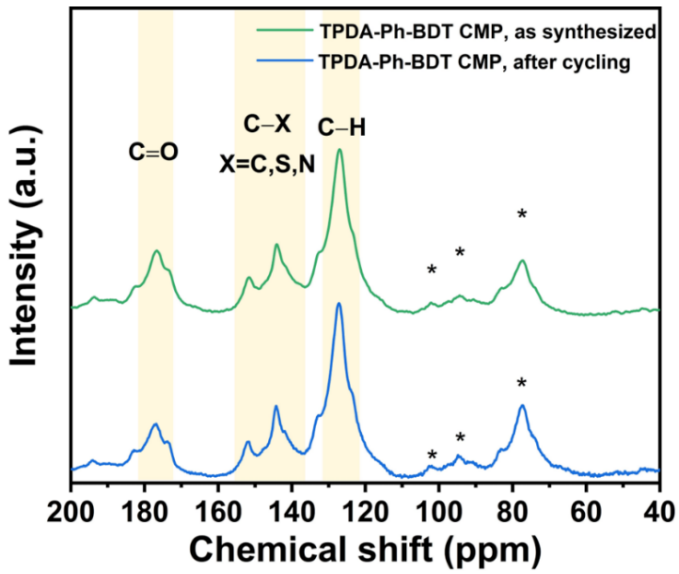

Figure S17. Solid-state ^{13}C CP/MAS NMR of the TPDA-Ph-BDT electrode before and after 50000 cycling.

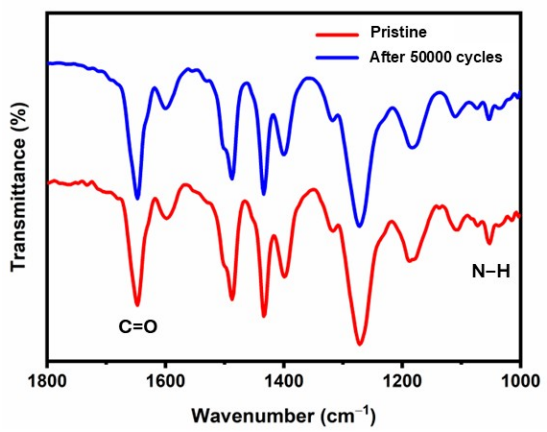

Figure S18. *Ex-situ* FT-IR spectrum of TPDA-Ph-BDT CMP electrode after 50000 cycles compared with that from the pristine electrode.

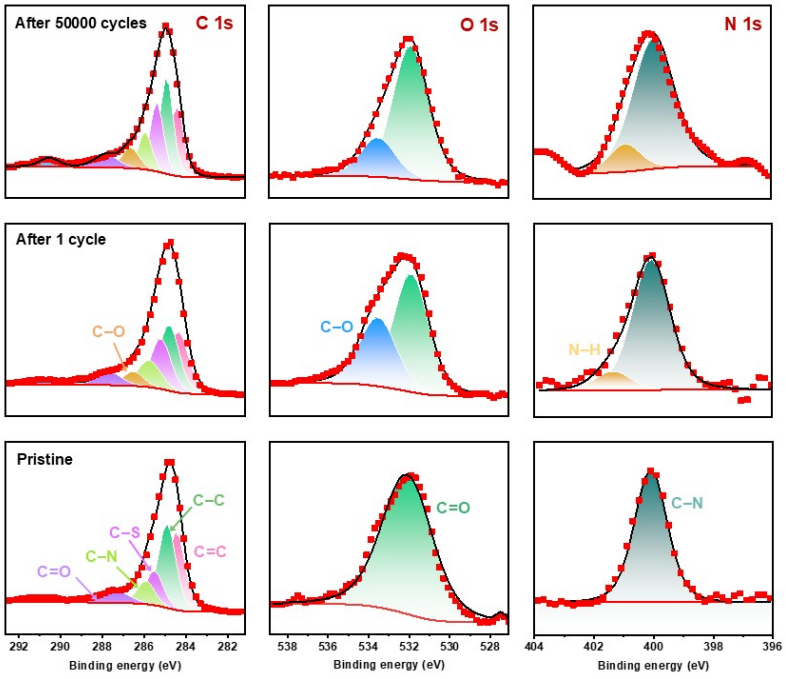

Figure S19. Deconvolution of the high-resolution XPS spectra of TPDA-Ph-BDT CMP electrodes after 1 cycle and 50000 cycles compared with that of the pristine electrode.

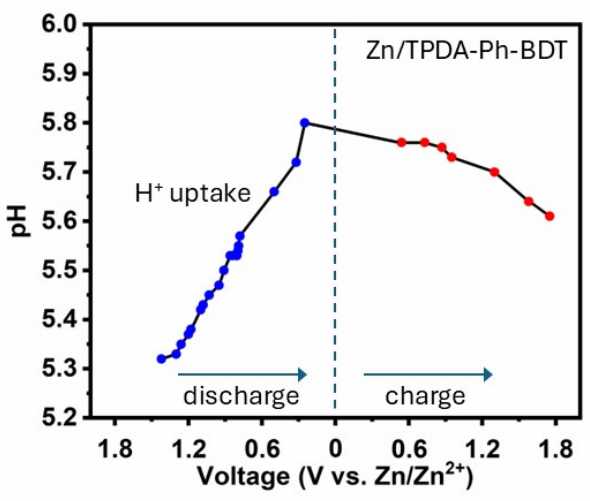

Figure S20. pH variation of the Zn/TPDA-Ph-BDT cell during the first cycle at 500 mA g^{-1}, confirming the involvement of H^+ in the redox reactions. The pH increase/decrease in the discharge/charge process, respectively, suggests reversible uptake/release of H^+ at different electrochemical states.

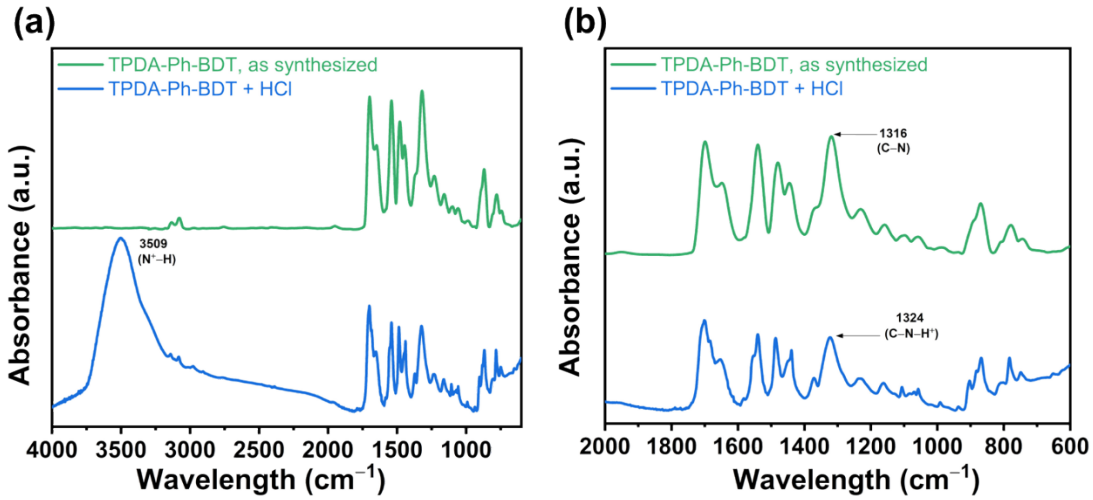

Figure S21. FTIR spectra of as-synthesized TPDA-Ph-BDT CMP and HCl-treated TPDA-Ph-BDT CMP. (a) The appearance of a broad N^+–H stretching band (~3509 cm^{-1}) and (b) the shift of the C–N stretching band from ~1316 to ~1324 cm^{-1} after HCl treatment support protonation of the amine N sites.

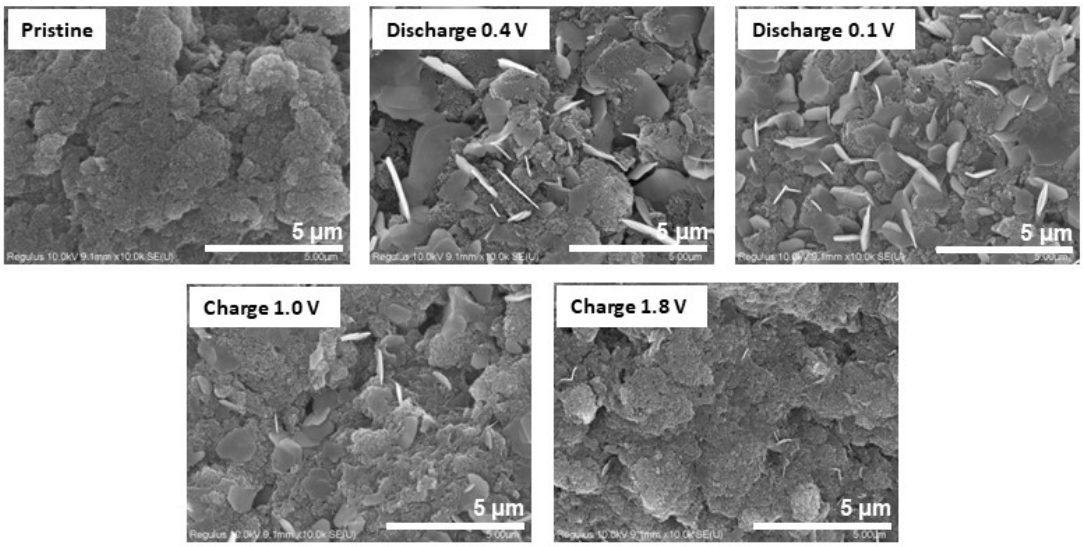

Figure S22. SEM images of TPDA-Ph-BDT CMP electrodes at different states of charge: pristine, discharge to 0.4 and 0.1 V, followed by charge to 1.0 and 1.8 V, showing various degrees of formation of flake-like zinc hydroxide sulfate (ZHS) on the electrode surface.

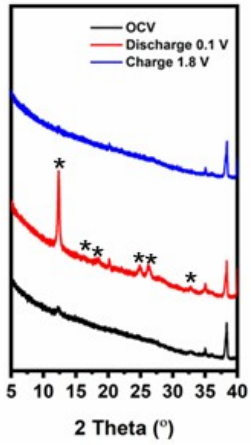

Figure S23. Ex-situ PXRD patterns of TPDA-Ph-BDT CMP electrodes at the end of discharge and end of charge compared to that at OCV (* indicates peaks from ZHS).

Temperature (°C)	R_{ct} (Ω)
30	2353
35	1755
40	1592
45	1042

Figure S24. Calculated R_{ct} values at the four temperatures analyzed on TPDA-Ph-BDT CMP aqueous cell using EIS.

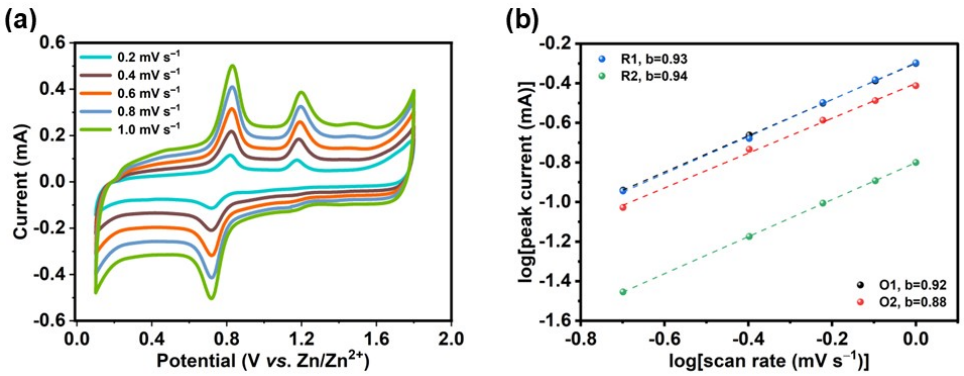

Figure S25. (a) CV curves of TPDA-Ph-BDT CMP electrode at various scan rates. (b) Relationship between log i (peak current) and log v (scan rate) from the CV curves in (a). The analysis of charge storage process was performed on the material with b values calculated from $i = av^b$.

S10. ICP-OES analysis of TPDA-Ph-BDT electrodes

Table S3. ICP-OES result of TPDA-Ph-BDT electrodes after discharge in zinc-organic batteries.

Sample	Pristine electrode (mg)	Discharged electrode (mg)	%Zn by ICP	%S by ICP	n($C_{74}N_2O_4S_4H_{40}$) (10^{-6} mol)	n_{ZHS} (10^{-4} mol)	n_{Zn2+} (10^{-7} mol)	C_{Zn2+} (mAh)	C_{Exp} (mAh)
1-$Dis_{0.1V}$	1.37	1.40	20.14	2.59	1.19	1.08	1.58	0.008	0.190
2-$Dis_{0.1V}$	1.63	1.71	30.19	3.82	1.42	1.99	0.38	0.002	0.209
3-$Dis_{0.1V}$	1.31	1.96	23.32	2.94	1.14	1.76	0.68	0.004	0.187

Note: ZHS = $Zn_4(OH)_5SO_4{\cdot}5H_2O$; n = mole; C_{Zn2+} = charge from inserted Zn^{2+} in mAh; C_{Exp} = total charge obtained experimentally from Zn-organic cell in mAh.

The capacity contribution from Zn^{2+} can be calculated as follows:

$$n_{Zn(ICP)} = \frac{\%Zn\ x\ [mass(discharged)\ in\ g]}{65\ \frac{g}{mol}}$$

$$n_{S(ICP)} = \frac{\%S\ x\ [mass(discharged)\ in\ g]}{32\ \frac{g}{mol}}$$

Where mass(discharged) is mass of discharged electrode in g; $n_{Zn(ICP)}$ is mole of total Zn from ICP; $n_{S(ICP)}$ is mole of total S from ICP; $C_{74}N_2O_4S_4H_{40}$ is formula of TPDA-Ph-BDT's repeating unit.

$$n_{S(ICP)} = n_{ZHS} + 4n(C_{74}N_2O_4S_4H_{40})$$

$$n_{ZHS} = n_{S(ICP)} - 4n(C_{74}N_2O_4S_4H_{40})$$

$$n_{Zn(ICP)} = n_{Zn2+} + 4n_{ZHS}$$

$$n_{Zn2+} = n_{Zn(ICP)} - 4n_{ZHS}$$

$$C_{Zn2+} = \frac{(2)(n_{Zn2+})(96500\ \frac{C}{mol})(1\ mAh)}{(3.6\ C)}$$

Capacity contribution from Zn^{2+} = $\frac{C_{Zn2+}}{C_{Exp}}$ x 100 %

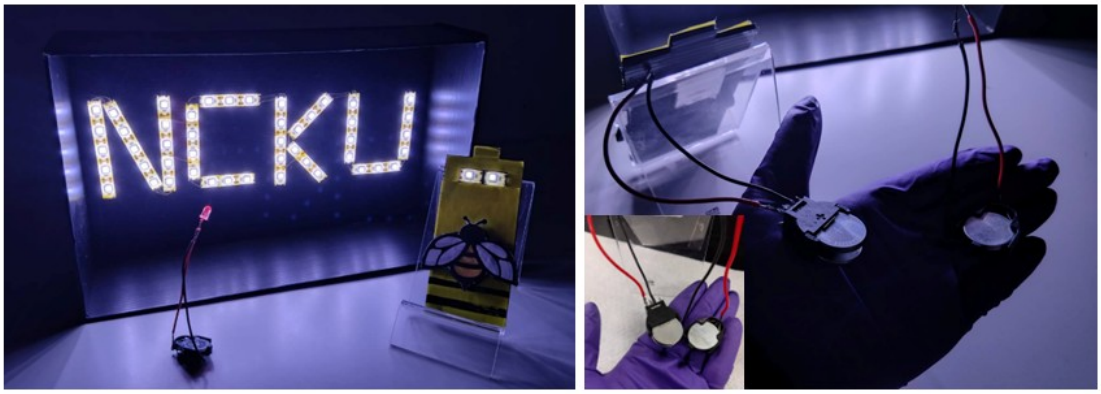

Figure S26. An image of the devices fabricated using the aqueous Zn-organic coin cells with TPDA-Ph-BDT cathode.

Table S4. Porous polymer and small-molecule organic cathode materials for aqueous zinc-organic batteries reported in the literature.

Structure	Composition of Electrode (**active material**: conductive carbon: binder)	Electrolyte	Theoretical Capacity (Electron Transfer)	Voltage Window (V)	Initial Capacity at Lowest Rate Reported	Reversible Capacity at Highest Rate Reported	Capacity Retention at Highest Rate (ED = energy density; PD = power density)	Ref.
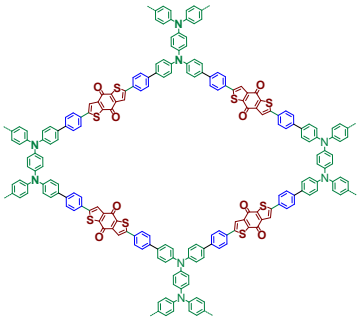	**TPDA-Ph-BDT CMP**:KB:PVDF (6:3:1)	1 M aqueous $ZnSO_4$	140 mAh g^{-1} (6 e^-)	0.1–1.8	154 mAh g^{-1} at 500 mA g^{-1}	85 mAh g^{-1} at 20 A g^{-1} (76 mAh g^{-1} at 45 A g^{-1} for 10 cycles)	96 % after 50000 cycles at 20 A g^{-1}	**This work**
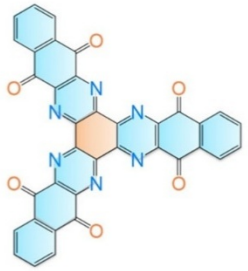	**HATNQ**:rGO:PVDF (6:3.5:0.5)	3 M aqueous $ZnSO_4$	515 mAh g^{-1} (12 e^-)	0.1–1.6	370 mAh g^{-1} at 200 mA g^{-1}	178 mAh g^{-1} at 9 A g^{-1}	0.0068% per cycle after 11000 cycles at 5 A g^{-1} (ED = 289 Wh kg^{-1}; PD = 119 W kg^{-1})	1

Structure	Composition of Electrode (**active material**: conductive carbon: binder)	Electrolyte	Theoretical Capacity (Electron Transfer)	Voltage Window (V)	Initial Capacity at Lowest Rate Reported	Reversible Capacity at Highest Rate Reported	Capacity Retention at Highest Rate (ED = energy density; PD = power density)	Ref.
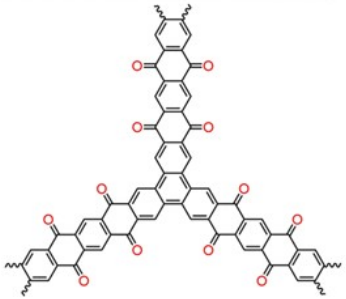	**rPOP**:SP:PTFE (7:2:1)	1 M aqueous $ZnSO_4$	N/A	0.1–1.6	120 mAh g^{-1} at 100 mA g^{-1}	26 mAh g^{-1} at 2 A g^{-1}	66 % after 30000 cycles at 2 A g^{-1}	2
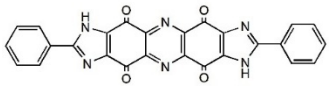	**PMTP@CNT-40**: MWCNTs:PVDF (7:2:1)	2 M aqueous $ZnSO_4$	439 mAh g^{-1} (18 e^-)	0.2–1.8	370 mAh g^{-1} at 100 mA g^{-1}	164 mAh g^{-1} at 10 A g^{-1}	64 % after 4000 cycles at 3 A g^{-1} (ED = 234 Wh kg^{-1}; PD = 81.5 W kg^{-1})	3

Structure	Composition of Electrode (**active material**: conductive carbon: binder)	Electrolyte	Theoretical Capacity (Electron Transfer)	Voltage Window (V)	Initial Capacity at Lowest Rate Reported	Reversible Capacity at Highest Rate Reported	Capacity Retention at Highest Rate (ED = energy density; PD = power density)	Ref.
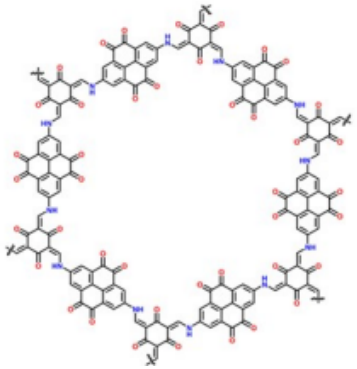	**Tp-PTO-COF**:SP:PVDF (6:3.5:0.5)	2 M aqueous $ZnSO_4$	439 mAh g^{-1} (18 e^-)	0.4–1.5	301 mAh g^{-1} at 200 mA g^{-1}	140 mAh g^{-1} at 10 A g^{-1}	95 % after 1000 cycles at 2 A g^{-1}	4
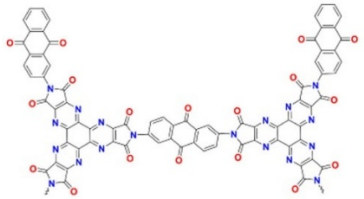	**HTAQ**:KB: PVDF (3:6:1)	2 M aqueous $ZnSO_4$	538 mAh g^{-1} (30 e^-)	0.1–1.45	294 mAh g^{-1} at 500 mA g^{-1}	89 mAh g^{-1} at 20 A g^{-1}	67 % after 1900 cycles at 2 A g^{-1} (ED = 8.7 Wh kg^{-1}; PD = 104 W kg^{-1})	5

Structure	**Composition of Electrode** (**active material**: conductive carbon: binder)	**Electrolyte**	**Theoretical Capacity (Electron Transfer)**	**Voltage Window (V)**	**Initial Capacity at Lowest Rate Reported**	**Reversible Capacity at Highest Rate Reported**	**Capacity Retention at Highest Rate (ED = energy density; PD = power density)**	**Ref.**
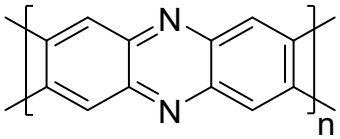	**PoPD**:AB:PVDF (7:2:1)	2 M aqueous $ZnSO_4$	301 mAh g^{-1} (2 e^-)	0.25–1.25	318 mAh g^{-1} at 50 mA g^{-1}	104 mAh g^{-1} at 1 A g^{-1} (95 mAh g^{-1} at 5 A g^{-1} for 5 cycles)*	66 % after 3000 cycles at 1 A g^{-1}	6
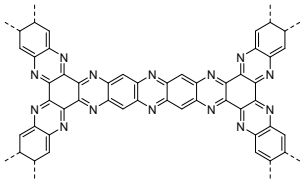	**PA-COF**:AB:PTFE (6:3:1)	1 M aqueous $ZnSO_4$	470 mAh g^{-1} (14 e^-)	0.2–1.6	247 mAh g^{-1} at 100 mA g^{-1}	95 mAh g^{-1} at 1 A g^{-1} (68 mAh g^{-1} at 10 A g^{-1} for 5 cycles)*	62 % after 10000 cycles at 1 A g^{-1}	7

Structure	Composition of Electrode (**active material**: conductive carbon: binder)	Electrolyte	Theoretical Capacity (Electron Transfer)	Voltage Window (V)	Initial Capacity at Lowest Rate Reported	Reversible Capacity at Highest Rate Reported	Capacity Retention at Highest Rate (ED = energy density; PD = power density)	Ref.
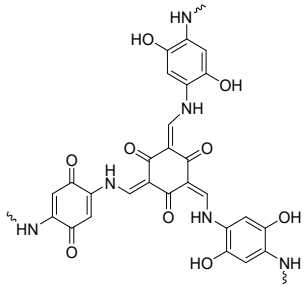	**HqTp-COF**:CNF (4:1)	3 M aqueous $ZnSO_4$	442 mAh g^{-1} (24 e^-)	0.2–1.8	276 mAh g^{-1} at 125 mA g^{-1}	81 mAh g^{-1} at 3.75 A g^{-1}	95 % after 1000 cycles at 3.75 A g^{-1} (ED = 240 Wh kg^{-1}; PD = 109 W kg^{-1})	8
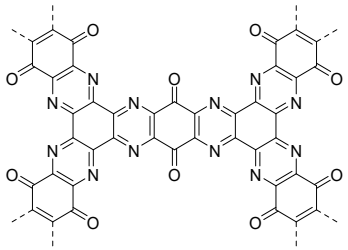	**HAQ-COF**:AB:PTFE (6:3:1)	2 M aqueous $ZnSO_4$	700 mAh g^{-1} (22 e^-)	0.2–1.6	344 mAh g^{-1} at 100 mA g^{-1}	170 mAh g^{-1} at 5 A g^{-1}	85 % after 10000 cycles at 5 A g^{-1}	9

Structure	Composition of Electrode (**active material**: conductive carbon: binder)	Electrolyte	Theoretical Capacity (Electron Transfer)	Voltage Window (V)	Initial Capacity at Lowest Rate Reported	Reversible Capacity at Highest Rate Reported	Capacity Retention at Highest Rate (ED = energy density; PD = power density)	Ref.
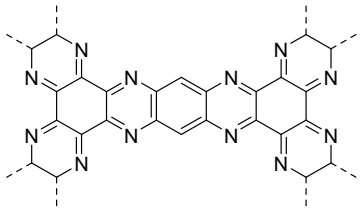	**HA-COF**:AB:PTFE (6:3:1)	2 M aqueous $ZnSO_4$	645 mAh g^{-1} (12 e^-)	0.2–1.6	164 mAh g^{-1} at 100 mA g^{-1}	50 mAh g^{-1} at 5 A g^{-1}	30 % after 10000 cycles at 5 A g^{-1}	9
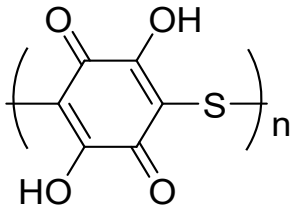	**PDBS**:AB:PVDF (8:1:1)	2 M aqueous $ZnSO_4$	268 mAh g^{-1} (2 e^-)	0.1–1.65	215 mAh g^{-1} at 50 mA g^{-1}	197 mAh g^{-1} at 2 A g^{-1}	~79 % after 2000 cycles (ED = 157 Wh kg^{-1}; PD = 31 W kg^{-1})	10

Structure	Composition of Electrode (**active material**: conductive carbon: binder)	Electrolyte	Theoretical Capacity (Electron Transfer)	Voltage Window (V)	Initial Capacity at Lowest Rate Reported	Reversible Capacity at Highest Rate Reported	Capacity Retention at Highest Rate (ED = energy density; PD = power density)	Ref.
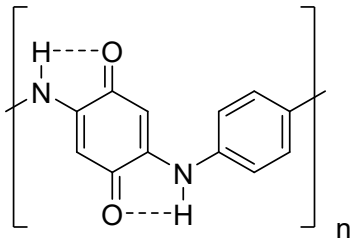	**PONEA**:GO:PTFE (3:6:1)	3 M aqueous $Zn(CF_3SO_3)_2$	222 mAh g^{-1} (2 e^-)	0.2–1.6	329 mAh g^{-1} at 100 mA g^{-1}	277 mAh g^{-1} at 10 A g^{-1} (270 mAh g^{-1} at 20 A g^{-1} for 5 cycles)*	85 % after 4800 cycles (ED = 242 Wh kg^{-1} at PD = 71 W kg^{-1})	11
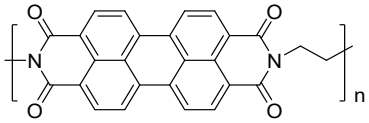	**PDI-EDA**/CB:PVDF (9:1)	2 M aqueous $ZnSO_4$	120 mAh g^{-1} (2 e^-)	0.1–1.2	118 mAh g^{-1} at 50 mA g^{-1}	98 mAh g^{-1} at 1 A g^{-1} (95 mAh g^{-1} at 5 A g^{-1} for 5 cycles)*	71 % after 1500 cycles at 1 A g^{-1}	12

Structure	Composition of Electrode (**active material**: conductive carbon: binder)	Electrolyte	Theoretical Capacity (Electron Transfer)	Voltage Window (V)	Initial Capacity at Lowest Rate Reported	Reversible Capacity at Highest Rate Reported	Capacity Retention at Highest Rate (ED = energy density; PD = power density)	Ref.
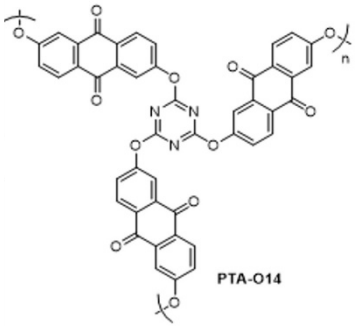 PTA-O14	**PTA-O14**:KB:PVDF (6:3:1)	3 M aqueous $ZnSO_4$	N/A	0.005–1.8	118 mAh g^{-1} at 50 mA g^{-1}	34 mAh g^{-1} at 200 mA g^{-1}	23 % after 200 cycles at 50 mA g^{-1}	13
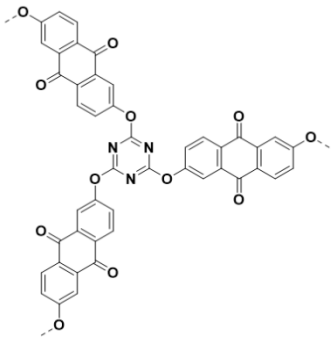	**PTA-O26**:KB:PVDF (6:3:1)	3 M aqueous $ZnSO_4$	N/A	0.005–1.8	296 mAh g^{-1} at 50 mA g^{-1}	130 mAh g^{-1} at 200 mA g^{-1}	92 % after 200 cycles at 50 mA g^{-1}	13

Structure	Composition of Electrode (**active material**: conductive carbon: binder)	Electrolyte	Theoretical Capacity (Electron Transfer)	Voltage Window (V)	Initial Capacity at Lowest Rate Reported	Reversible Capacity at Highest Rate Reported	Capacity Retention at Highest Rate (ED = energy density; PD = power density)	Ref.
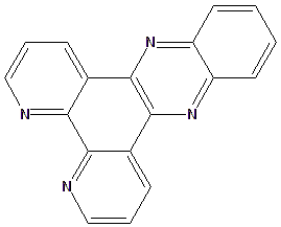	**DPPZ**:KB:PTFE (6:3:1)	Saturated aqueous $ZnSO_4$	379 mAh g^{-1} (4 e^-)	0.3–1.4	94 mAh g^{-1} at 500 mA g^{-1}	40 mAh g^{-1} at 5 A g^{-1}	77% after 8000 cycles at 5 A g^{-1}	14
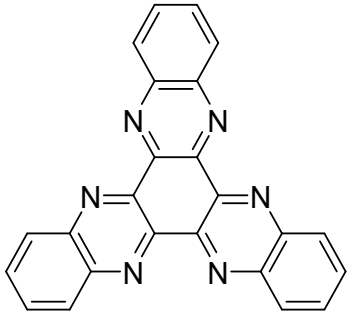	**DQP**:KB:PTFE (6:3:1)	1 M aqueous $ZnSO_4$	418 mAh g^{-1} (6 e^-)	0.2–1.4	413 mAh g^{-1} at 50 mA g^{-1}	162 mAh g^{-1} at 5 A g^{-1}	86 % after 1000 cycles at 5 A g^{-1} (ED = 220 Wh kg^{-1}; PD = 25 W kg^{-1})	15

Structure	Composition of Electrode (**active material**: conductive carbon: binder)	Electrolyte	Theoretical Capacity (Electron Transfer)	Voltage Window (V)	Initial Capacity at Lowest Rate Reported	Reversible Capacity at Highest Rate Reported	Capacity Retention at Highest Rate (ED = energy density; PD = power density)	Ref.
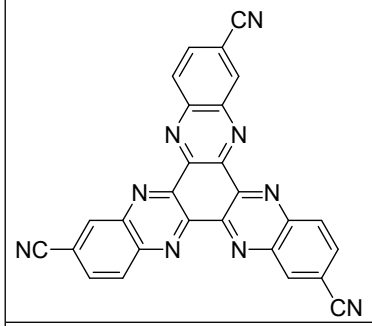	**HATN-3CN**:KB:PVDF (6:3:1)	2 M aqueous $ZnSO_4$	350 mAh g^{-1} (6 e^-)	0.1–1.6	320 mAh g^{-1} at 50 mA g^{-1}	240 mAh g^{-1} at 5 A g^{-1} (~180 mAh g^{-1} at 20 A g^{-1} for 5 cycles)*	~91 % after 5800 cycles at 5 A g^{-1} (ED = 149.3 Wh kg^{-1}; PD = 24.1 W kg^{-1})	16
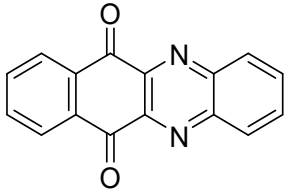	**BPD**:KB:PVDF (6:3:1)	2 M aqueous $ZnSO_4$	412 mAh g^{-1} (4 e^-)	0.2–1.3	429 mAh g^{-1} at 50 mA g^{-1}	135.2 mAh g^{-1} at 5 A g^{-1}	73 % after 10000 cycles at 5 A g^{-1} (ED = 276 Wh kg^{-1} at PD = 21.1 W kg^{-1})	17

Structure	Composition of Electrode (**active material**: conductive carbon: binder)	Electrolyte	Theoretical Capacity (Electron Transfer)	Voltage Window (V)	Initial Capacity at Lowest Rate Reported	Reversible Capacity at Highest Rate Reported	Capacity Retention at Highest Rate (ED = energy density; PD = power density)	Ref.
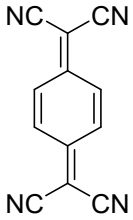	**TCNQ**:SP:PTFE (6:3:1)	2 M aqueous $ZnSO_4$	262 mAh g^{-1} (2 e^-)	0.6–1.8	192 mAh g^{-1} at 20 mA g^{-1}	116 mAh g^{-1} at 100 mA g^{-1}	65 % after 100 cycles at 100 mA g^{-1}	18
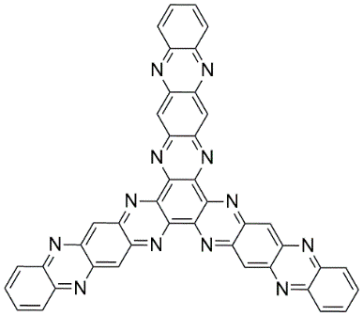	**HATN-PNZ**:AB:PVDF (6:3:1)	2 M aqueous $ZnSO_4$	466 mAh g^{-1} (12 e^-)	0.1–1.6	257 mAh g^{-1} at 500 mA g^{-1}	159 mAh g^{-1} at 30 A g^{-1}	93 % after 30000 cycles at 30 A g^{-1} (ED = 153.9 Wh kg^{-1}; PD = 2.5 W kg^{-1})	19

Structure	Composition of Electrode (**active material**: conductive carbon: binder)	Electrolyte	Theoretical Capacity (Electron Transfer)	Voltage Window (V)	Initial Capacity at Lowest Rate Reported	Reversible Capacity at Highest Rate Reported	Capacity Retention at Highest Rate (ED = energy density; PD = power density)	Ref.
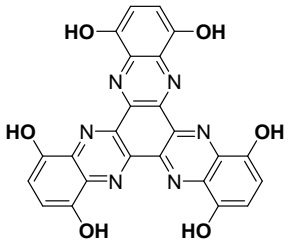	**TQD**:CB:PTFE (6:3:1)	4 M aqueous $ZnSO_4$	669 mAh g^{-1} (12 e^-)	0.25–1.5	503 mAh g^{-1} at 100 mA g^{-1}	310 mAh g^{-1} at 1 A g^{-1} (84 mAh g^{-1} at 5 A g^{-1} for 10 cycles in the voltage range of 0.4 – 1.5 V)	71 % after 400 cycles at 1 A g^{-1} in the voltage range of 0.4 – 1.5 V	20
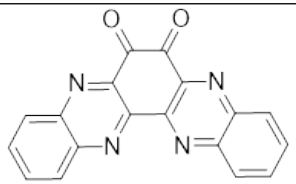	**ODQC**:PTX:PVDF (6:3:1)	3 M aqueous $ZnSO_4$	515 mAh g^{-1} (6 e^-)	0.25–1.6	159 mAh g^{-1} at 50 mA g^{-1}	~142 mAh g^{-1} at 50 mA g^{-1}	89 % after 100 cycles at 50 mA g^{-1}	21
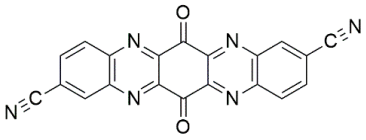	**DCTPQ**:KB:PTFE (6:3:1)	2 M aqueous $ZnSO_4$	441 mAh g^{-1} (6 e^-)	0.1–1.4	244 mAh g^{-1} at 300 mA g^{-1}	~50 mAh g^{-1} at 500 mA g^{-1}	50 % after 210 cycles at 500 mA g^{-1}	22

Structure	Composition of Electrode (**active material**: conductive carbon: binder)	Electrolyte	Theoretical Capacity (Electron Transfer)	Voltage Window (V)	Initial Capacity at Lowest Rate Reported	Reversible Capacity at Highest Rate Reported	Capacity Retention at Highest Rate (ED = energy density; PD = power density)	Ref.
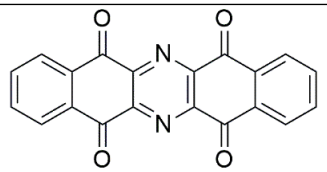	**DBPTQ**:KB:PVDF (6:3:1)	2 M aqueous $ZnSO_4$	472 mAh g^{-1} (6 e^-)	0.2–1.4	382 mAh g^{-1} at 50 mA g^{-1}	98 mAh g^{-1} at 5 A g^{-1}	62 % after 60000 cycles at 5 A g^{-1} (ED = 227 Wh kg^{-1})	23
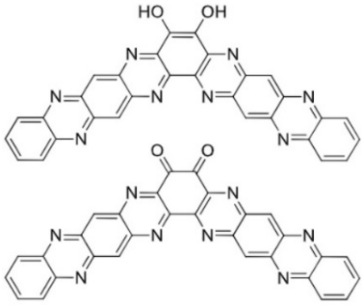	**TQC**:PTX: PTFE (6:3:1)	3 M aqueous $ZnSO_4$	310 mAh g^{-1} (6 e^-) 517 mAh g^{-1} (10 e^-)	0.25–1.6	301 mAh g^{-1} at 50 mA g^{-1}	~214 mAh g^{-1} at 100 mA g^{-1}	71 % after 100 cycles at 50 mA g^{-1}	21

Structure	**Composition of Electrode (active material**: conductive carbon: binder)	**Electrolyte**	**Theoretical Capacity (Electron Transfer)**	**Voltage Window (V)**	**Initial Capacity at Lowest Rate Reported**	**Reversible Capacity at Highest Rate Reported**	**Capacity Retention at Highest Rate (ED = energy density; PD = power density)**	**Ref.**
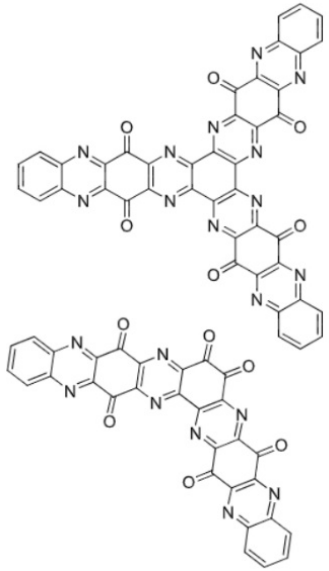	**QTQC**:PTX:PTFE (6:3:1)	3 M aqueous $ZnSO_4$	trimer OTQC 619 mAh g^{-1} (20 e^-) dimer OTQC 651 mAh g^{-1} (14 e^-)	0.25−1.6	326 mAh g^{-1} at 100 mA g^{-1}	~200 mAh g^{-1} at 100 mA g^{-1} ~140 mAh g^{-1} at 100 mA g^{-1}	60 % after 100 cycles at 100 mA g^{-1} 42 % after 400 cycles at 100 mA g^{-1}	24

Structure	Composition of Electrode (**active material**: conductive carbon: binder)	Electrolyte	Theoretical Capacity (Electron Transfer)	Voltage Window (V)	Initial Capacity at Lowest Rate Reported	Reversible Capacity at Highest Rate Reported	Capacity Retention at Highest Rate (ED = energy density; PD = power density)	Ref.
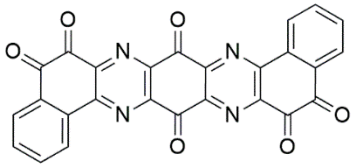	**BBQPH**:KB:PVDF (6:3:1)	3 M aqueous $ZnSO_4$	567 mAh g^{-1} (8 e^-)	0.2–1.6	499 mAh g^{-1} at 200 mA g^{-1}	~380 mAh g^{-1} at 5 A g^{-1}	95 % after 1000 cycles at 5 A g^{-1} (ED = 355 Wh kg^{-1})	25
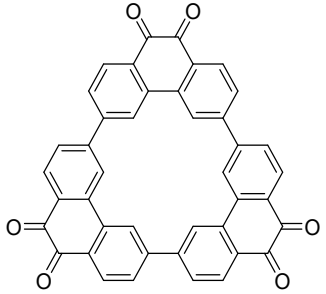	**PQ-Δ**:AB:PVDF (6:3:1)	3 M aqueous $Zn(CF_3SO_3)_2$	216 mAh g^{-1} (2 e^-)	0.25–1.6	~200 mAh g^{-1} at 30 mA g^{-1}	~210 mAh g^{-1} at 150 mA g^{-1}	~99.9 % after 500 cycles at 150 mA g^{-1}	26

Structure	Composition of Electrode (**active material**: conductive carbon: binder)	Electrolyte	Theoretical Capacity (Electron Transfer)	Voltage Window (V)	Initial Capacity at Lowest Rate Reported	Reversible Capacity at Highest Rate Reported	Capacity Retention at Highest Rate (ED = energy density; PD = power density)	Ref.
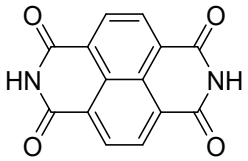	**NDI**:SP:PVDF (6:3:1)	1 M aqueous $ZnSO_4$	202 mAh g^{-1} (2 e^-)	0.2–1.0	~223 mAh g^{-1} at 202 mA g^{-1}	~100 mAh g^{-1} at 202 mA g^{-1} (~25 mAh g^{-1} at 2020 mA g^{-1} for 5 cycles)*	45 % after 100 cycles at 202 mA g^{-1}	27
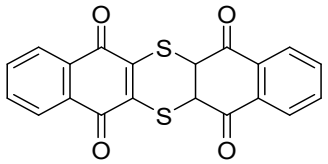	**DTT**:KB:PTFE (6:3:1)	2 M aqueous $ZnSO_4$	285 mAh g^{-1} (4 e^-)	0.3–1.4	211 mAh g^{-1} at 50 mA g^{-1}	~78 mAh g^{-1} at 2 A g^{-1}	83 % after 23000 cycles at 2 A g^{-1} (ED = 1267 Wh kg^{-1}; PD = 312 W kg^{-1})	28

Structure	Composition of Electrode (**active material**: conductive carbon: binder)	Electrolyte	Theoretical Capacity (Electron Transfer)	Voltage Window (V)	Initial Capacity at Lowest Rate Reported	Reversible Capacity at Highest Rate Reported	Capacity Retention at Highest Rate (ED = energy density; PD = power density)	Ref.
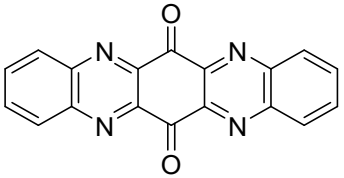	**TAPQ**:KB:PTFE (6:3:1)	1 M aqueous $ZnSO_4$	515 mAh g^{-1} (6 e^-)	0.1–1.6	443 mAh g^{-1} at 50 mA g^{-1}	222 mAh g^{-1} at 50 mA g^{-1} (~20 mAh g^{-1} at 5 A g^{-1} for 10 cycles)*	50 % after 100 cycles at 50 mA g^{-1} (ED = 227 Wh kg^{-1})	29
				0.3–1.6	325 mAh g^{-1} at 50 mA g^{-1}	282 mAh g^{-1} at 50 mA g^{-1} (~30 mAh g^{-1} at 5 A g^{-1} for 10 cycles)*	87 % after 100 cycles at 50 mA g^{-1}	

Structure	Composition of Electrode (**active material**: conductive carbon: binder)	Electrolyte	Theoretical Capacity (Electron Transfer)	Voltage Window (V)	Initial Capacity at Lowest Rate Reported	Reversible Capacity at Highest Rate Reported	Capacity Retention at Highest Rate (ED = energy density; PD = power density)	Ref.
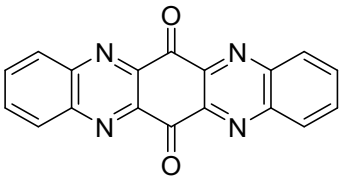	**TAPQ**:KB:PTFE (6:3:1)	1 M aqueous $ZnSO_4$	515 mAh g^{-1} (6 e^-)	0.5–1.6	270 mAh g^{-1} at 50 mA g^{-1}	182 mAh g^{-1} at 2 A g^{-1} (~70 mAh g^{-1} at 5 A g^{-1} for 10 cycles)*	97 % after 100 cycles at 50 mA g^{-1} (ED = 282 Wh kg^{-1}) 69 % after 1000 cycles at 2 A g^{-1}	29
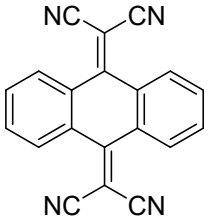	**TCNAQ**:SP:PTFE (6:3:1)	2 M aqueous $ZnSO_4$	176 mAh g^{-1} (2 e^-)	0.6–1.8	169 mAh g^{-1} at 20 mA g^{-1}	95 mAh g^{-1} at 500 mA g^{-1} (55 mAh g^{-1} at 1 A g^{-1} for 10 cycles)*	81 % after 1000 cycles at 500 mA g^{-1}	18

Structure	**Composition of Electrode** (**active material**: conductive carbon: binder)	**Electrolyte**	**Theoretical Capacity (Electron Transfer)**	**Voltage Window (V)**	**Initial Capacity at Lowest Rate Reported**	**Reversible Capacity at Highest Rate Reported**	**Capacity Retention at Highest Rate (ED = energy density; PD = power density)**	**Ref.**
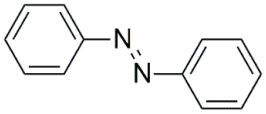	**AZOB**:SP:PTFE (6:3:1)	2 M aqueous $ZnSO_4$	294 mAh g^{-1} (4 e^-)	0.3–1.4	200 mAh g^{-1} at 50 mA g^{-1}	150 mAh g^{-1} at 800 mA g^{-1}	N/A ED = 120 Wh kg^{-1}; PD = 62.9 W kg^{-1}	30
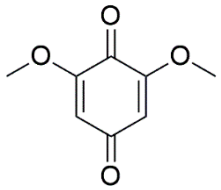	***m*-DMBQ**:SP:PTFE (6:3:1)	2 M aqueous $ZnSO_4$	319 mAh g^{-1} (4 e^-)	0.4–1.5	312 mAh g^{-1} at 200 mA g^{-1}	~150 mAh g^{-1} at 20 A g^{-1}	75 % after 4000 cycles at 20 A g^{-1} (ED = 275 Wh kg^{-1})	30

Structure	Composition of Electrode (**active material**: conductive carbon: binder)	Electrolyte	Theoretical Capacity (Electron Transfer)	Voltage Window (V)	Initial Capacity at Lowest Rate Reported	Reversible Capacity at Highest Rate Reported	Capacity Retention at Highest Rate (ED = energy density; PD = power density)	Ref.
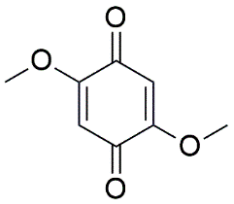	***p*-DMBQ**:SP:PTFE (6:3:1)	2 M aqueous $ZnSO_4$	319 mAh g^{-1} (4 e^-)	0.4–1.5	266 mAh g^{-1} at 200 mA g^{-1}	N/A	62 % after 5 cycles at 5 A g^{-1}	31
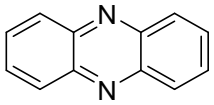	**PNZ**:KB:PTFE (6:3:1)	2 M aqueous $ZnSO_4$	297 mAh g^{-1} (2 e^-)	0.45–1.7	232 mAh g^{-1} at 20 mA g^{-1}	85 mAh g^{-1} at 1 A g^{-1}	79 % after 1000 cycles at 1 A g^{-1} (ED = 153 Wh kg^{-1}; PD= 44 W kg^{-1})	30

Structure	Composition of Electrode (**active material**: conductive carbon: binder)	Electrolyte	Theoretical Capacity (Electron Transfer)	Voltage Window (V)	Initial Capacity at Lowest Rate Reported	Reversible Capacity at Highest Rate Reported	Capacity Retention at Highest Rate (ED = energy density; PD = power density)	Ref.
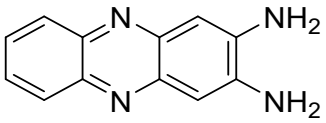	**DAP**:KB:PTFE (6:3:1)	2 M aqueous $ZnSO_4$	254 mAh g^{-1} (4 e^-)	0.45–1.7	213 mAh g^{-1} at 20 mA g^{-1}	28 mAh g^{-1} at 100 mA g^{-1}	29 % after 200 cycles at 100 mA g^{-1}	32
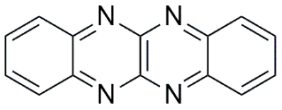	**TANC**:KB:PTFE (6:3:1)	3 M $Zn(CF_3SO_3)_2$	230 mAh g^{-1} (2 e^-)	0.8–1.4	213 mAh g^{-1} at 115 mA g^{-1}	121 mAh g^{-1} at 2.3 A g^{-1}	71 % after 47500 cycles at 2.3 A g^{-1} (ED = 245 Wh kg^{-1})	33

Structure	Composition of Electrode (**active material**: conductive carbon: binder)	Electrolyte	Theoretical Capacity (Electron Transfer)	Voltage Window (V)	Initial Capacity at Lowest Rate Reported	Reversible Capacity at Highest Rate Reported	Capacity Retention at Highest Rate (ED = energy density; PD = power density)	Ref.
	s-NMP-TCB-V2O5:SP:PVDF (6:3:1)	3 M $Zn(CF_3SO_3)_2$	218 mAh g^{-1} (2 e^-)	0.1–1.6	~450 mAh g^{-1} at ~500 mA g^{-1}	210 mAh g^{-1} at 10 A g^{-1}	85 % after 1500 cycles at 3 A g^{-1}	34
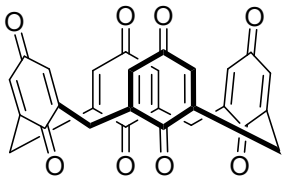	**C4Q**:SP:PVDF (6:3.5:0.5)	3 M aqueous $Zn(CF_3SO_3)_2$	446 mAh g^{-1} (8 e^-)	0.2–1.8	335 mAh g^{-1} at 20 mA g^{-1}	174 mAh g^{-1} at 500 mA g^{-1} (172 mAh g^{-1} at 1 A g^{-1} for 5 cycles)*	87 % after 1000 cycles at 500 mA g^{-1} (ED = 220 Wh kg^{-1} for pouch cell)	35

Structure	Composition of Electrode (**active material**: conductive carbon: binder)	Electrolyte	Theoretical Capacity (Electron Transfer)	Voltage Window (V)	Initial Capacity at Lowest Rate Reported	Reversible Capacity at Highest Rate Reported	Capacity Retention at Highest Rate (ED = energy density; PD = power density)	Ref.
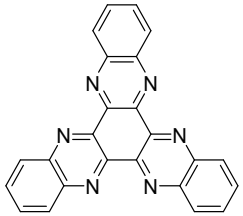	**HATN**:SP:PVDF (6:3.5:0.5)	2 M aqueous $ZnSO_4$	418 mAh g^{-1} (6 e^-)	0.3–1.1	405 mAh g^{-1} at 100 mA g^{-1}	140 mAh g^{-1} at 5 A g^{-1} (123 mAh g^{-1} at 20 A g^{-1} for 10 cycles)*	93 % after 5000 cycles at 5 A g^{-1}	36
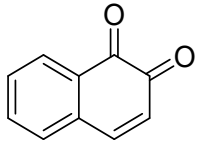	**1,2-NQ**:SP:PVDF (6:3.5:0.5)	3 M aqueous $Zn(CF_3SO_3)_2$	339 mAh g^{-1} (2 e^-)	0.2–1.8	~69 mAh g^{-1} at 20 mA g^{-1}	~51 mAh g^{-1} at 20 mA g^{-1}	~74 % after 5 cycles at 20 mA g^{-1}	35

Structure	Composition of Electrode (**active material**: conductive carbon: binder)	Electrolyte	Theoretical Capacity (Electron Transfer)	Voltage Window (V)	Initial Capacity at Lowest Rate Reported	Reversible Capacity at Highest Rate Reported	Capacity Retention at Highest Rate (ED = energy density; PD = power density)	Ref.
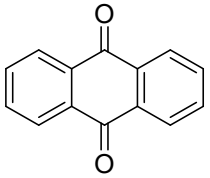	**9,10-AQ**:SP:PVDF (6:3.5:0.5)	3 M aqueous $Zn(CF_3SO_3)_2$	258 mAh g^{-1} (2 e^-)	0.2–1.8	~195 mAh g^{-1} at 20 mA g^{-1}	~125 mAh g^{-1} at 20 mA g^{-1}	~64 % after 40 cycles at 20 mA g^{-1}	35
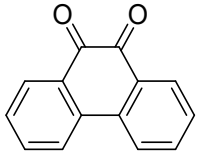	**9,10-PQ**:SP:PVDF (6:3.5:0.5)	3 M aqueous $Zn(CF_3SO_3)_2$	258 mAh g^{-1} (2 e^-)	0.2–1.8	~111 mAh g^{-1} at 20 mA g^{-1}	~88 mAh g^{-1} at 20 mA g^{-1}	~79 % after 5 cycles at 20 mA g^{-1}	35
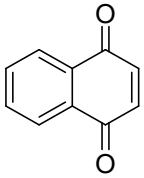	**1,4-NQ**:SP:PVDF (6:3.5:0.5)	3 M aqueous $Zn(CF_3SO_3)_2$	339 mAh g^{-1} (2 e^-)	0.2–1.8	~150 mAh g^{-1} at 20 mA g^{-1}	~48 mAh g^{-1} at 20 mA g^{-1}	~32 % after 5 cycles at 20 mA g^{-1}	35

Structure	Composition of Electrode (**active material**: conductive carbon: binder)	Electrolyte	Theoretical Capacity (Electron Transfer)	Voltage Window (V)	Initial Capacity at Lowest Rate Reported	Reversible Capacity at Highest Rate Reported	Capacity Retention at Highest Rate (ED = energy density; PD = power density)	Ref.
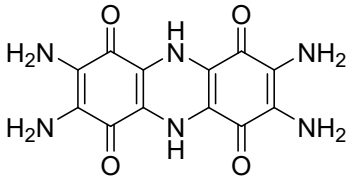	**TDT**: KB:PTFE (8:1:1)	1 M aqueous $ZnSO_4$	355 mAh g^{-1} (4 e^-)	0.1–1.75	369 mAh g^{-1} at 100 mA g^{-1}	182 mAh g^{-1} at 10 A g^{-1}	81 % after 3000 cycles at 10 A g^{-1}	37
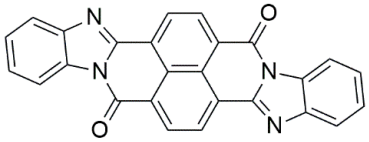	**BBPD**:CB:PTFE (8:1:1)	2 M aqueous $ZnSO_4$	130 mAh g^{-1} (2 e^-)	0.4–1.3	127 mAh g^{-1} at 100 mA g^{-1}	88 mAh g^{-1} at 20 A g^{-1}	90.7 % after 10000 cycles at 20 A g^{-1} (PD = 13.4 W kg^{-1})	38

Structure	Composition of Electrode (**active material**: conductive carbon: binder)	Electrolyte	Theoretical Capacity (Electron Transfer)	Voltage Window (V)	Initial Capacity at Lowest Rate Reported	Reversible Capacity at Highest Rate Reported	Capacity Retention at Highest Rate (ED = energy density; PD = power density)	Ref.
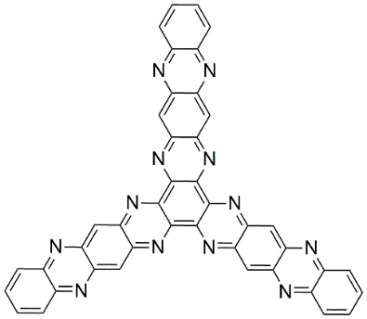	**TPHATP**: KB:PTFE (7:2:1)	2 M aqueous $ZnSO_4$	466 mAh g^{-1} (12 e^-)	0.2–1.7	318 mAh g^{-1} at 100 mA g^{-1}	109 mAh g^{-1} at 10 A g^{-1}	97 % after 5000 cycles at 10 A g^{-1} (ED = 178.1 Wh kg^{-1}; PD = 107.8 W kg^{-1})	39
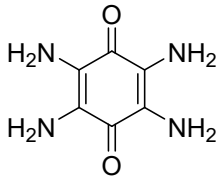	**TABQ**: KB: PVDF (5:4:1)	1 M aqueous $ZnSO_4$	319 mAh g^{-1} (2 e^-)	0.4–1.3	303 mAh g^{-1} at 100 mA g^{-1}	~240 mAh g^{-1} at 5 A g^{-1}	~89 % after 1000 cycles at 5 A g^{-1}	40

Structure	Composition of Electrode (**active material**: conductive carbon: binder)	Electrolyte	Theoretical Capacity (Electron Transfer)	Voltage Window (V)	Initial Capacity at Lowest Rate Reported	Reversible Capacity at Highest Rate Reported	Capacity Retention at Highest Rate (ED = energy density; PD = power density)	Ref.
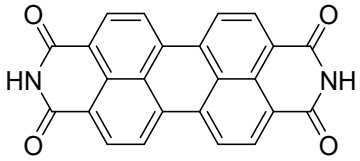	**PTCDI**:rGO:PVDF (7:2:1)	3 M aqueous $ZnSO_4$	135 mAh g^{-1} (2 e^-)	0.2–1.8	127 mAh g^{-1} at 50 mA g^{-1}	130 mAh g^{-1} at 3 A g^{-1} (121 mAh g^{-1} at 5 A g^{-1} for 10 cycles)*	97 % after 1500 cycles at 3 A g^{-1} (ED = 44 Wh kg^{-1})	41
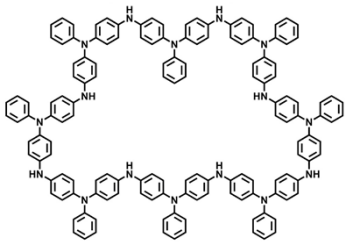	**m-PTPA**:CB:PVDF (8:1:1)	2 m aqueous $ZnCl_2$	253 mAh g^{-1}	0.6–1.7	210.7 mAh g^{-1} at 0.5 A g^{-1}	88 mAh g^{-1} at 6 A g^{-1}	87.6% after 1000 cycles at 6 A g^{-1} (ED = 236.0 Wh kg^{-1} at 0.6 kW kg^{-1}; PD = 6.8 kW kg^{-1} at 122.5 Wh kg^{-1})	42

Structure	Composition of Electrode (**active material**: conductive carbon: binder)	Electrolyte	Theoretical Capacity (Electron Transfer)	Voltage Window (V)	Initial Capacity at Lowest Rate Reported	Reversible Capacity at Highest Rate Reported	Capacity Retention at Highest Rate (ED = energy density; PD = power density)	Ref.
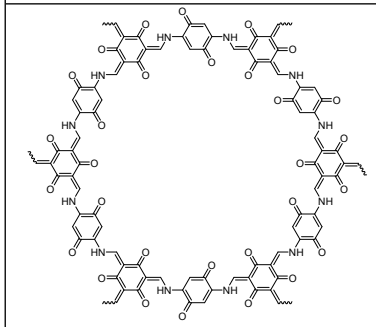	**PTO-HqTp COF**:CNF with 5wt% Nafion (4:1)	3 M aqueous $ZnSO_4$	442 mAh g^{-1} (24 e^-)	0.2–1.8	276 mAh g^{-1} at 125 mA g^{-1}	85 mAh g^{-1} at 3.75 A g^{-1}	95% after 1000 cycles at 3.75 A g^{-1} (ED = 240 Wh kg^{-1}; PD = 109 W kg^{-1})	43
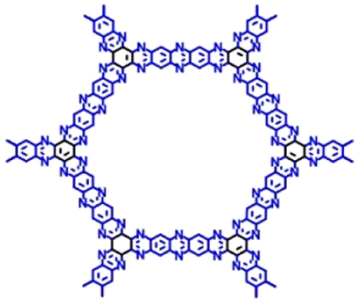	**PA-COF**:AB:PTFE (6:3:1)	3 M aqueous $ZnSO_4$	N/A	0.2–1.6	247 mAh g^{-1} at 0.1 A g^{-1}	93 mAh g^{-1} at 1 A g^{-1} (68 mAh g^{-1} at 10 A g^{-1} for 5 cycles)*	74% after 10000 cycles at 1.0 A g^{-1}	44

Structure	Composition of Electrode (**active material**: conductive carbon: binder)	Electrolyte	Theoretical Capacity (Electron Transfer)	Voltage Window (V)	Initial Capacity at Lowest Rate Reported	Reversible Capacity at Highest Rate Reported	Capacity Retention at Highest Rate (ED = energy density; PD = power density)	Ref.
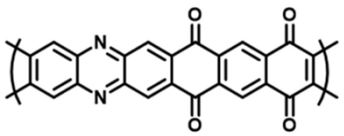	**PPPA**:KB:PVDF (7:2:1)	2 M aqueous $Zn(CF_3SO_3)_2$	442 mAh g^{-1} (6 e^-)	0.2–1.8	210.2 mAh g^{-1} at 50 mA g^{-1}	139.7 mAh g^{-1} at 5000 mA g^{-1}	70.6% after 20000 cycles at 5000 mA g^{-1}	45
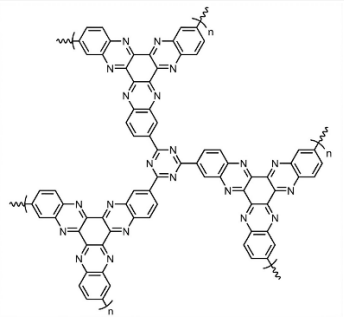	**P3Q-t**:AB:PTFE (6:3:1)	2 M aqueous $ZnSO_4$	N/A	0.1–1.6	237 mAh g^{-1} at 0.3 A g^{-1}	133 mAh g^{-1} at 3 A g^{-1} (50 mAh g^{-1} at 20 A g^{-1} for 5 cycles)*	81% after 1500 cycles at 3 A g^{-1}	46

Structure	Composition of Electrode (**active material**: conductive carbon: binder)	Electrolyte	Theoretical Capacity (Electron Transfer)	Voltage Window (V)	Initial Capacity at Lowest Rate Reported	Reversible Capacity at Highest Rate Reported	Capacity Retention at Highest Rate (ED = energy density; PD = power density)	Ref.
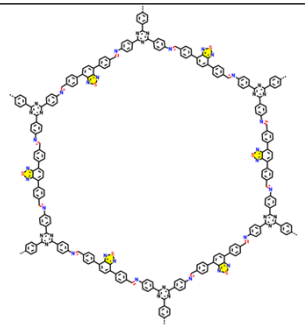	**COF-TMT-BT**: MWCNT:PTFE (7:2:1)	2 M aqueous $Zn(CF_3SO_3)_2$	N/A	0.5–1.6	283.5 mAh g^{-1} at 0.1 A g^{-1}	186.8 mAh g^{-1} at 0.1 A g^{-1} (146.2 mAh g^{-1} at 2 A g^{-1} for 10 cycles)*	65.9% after 2000 cycles at 0.1 A g^{-1} (ED = 219.6 Wh kg^{-1}; PD = 23.2 kW kg^{-1})	47
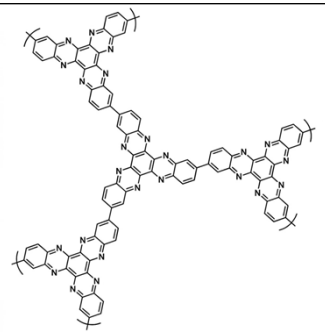	**P3Q**:SP:PVDF (6:3:1)	2 M aqueous $ZnSO_4$	N/A	0.1–1.6	226 mAh g^{-1} at 0.3 A g^{-1}	67 mAh g^{-1} at 3 A g^{-1} (100 mAh g^{-1} at 5 A g^{-1} for 5 cycles)*	68% after 1000 cycles at 3 A g^{-1}	48

Structure	Composition of Electrode (**active material**: conductive carbon: binder)	Electrolyte	Theoretical Capacity (Electron Transfer)	Voltage Window (V)	Initial Capacity at Lowest Rate Reported	Reversible Capacity at Highest Rate Reported	Capacity Retention at Highest Rate (ED = energy density; PD = power density)	Ref.
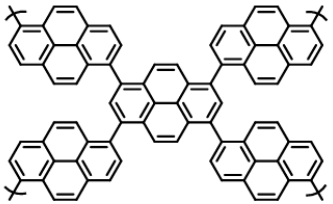 CL16Py	**CLPy**:KB:PVDF (5:3:2)	30 m aqueous $ZnCl_2$	N/A	0.6–1.8	180 mAh g^{-1} at 50 mA g^{-1}	105 mAh g^{-1} at 3000 mA g^{-1}	96.4% after 38000 cycles at 3 A g^{-1}	49
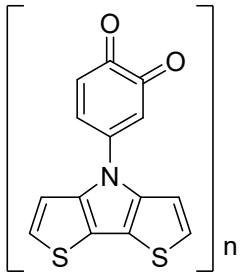	**PDpBQy**:AB:PTFE (7:2:1)	2 M aqueous $ZnSO_4$	N/A	0.9–1.6	120 mAh g^{-1} at 0.1 A g^{-1}	N/A (63 mAh g^{-1} at 5 A g^{-1} for 5 cycles)*	78% after 500 cycles at 2 A g^{-1} (ED = 139 Wh kg^{-1})	50

Note: * indicates capacity taken from the rate capability plot or the discharge/charge profile. KB = Ketjen black; CB = carbon black; AB = acetylene black; SP = Super P; rGO = reduced graphene oxide; MWCNTs = multiwall carbon nanotubes; GO = graphene oxide; PVDF = polyvinylidene fluoride; PTFE = polytetrafluoroethylene; La133 = polyacrylonitrile copolymer; DOL = 1,3-dioxolane; DME = dimethoxyethane; DMC = dimethyl carbonate; DEC = diethyl carbonate; EC = ethylene carbonate; EMC = ethyl methyl carbonate; PC = propylene carbonate; PTX = Printex XE2 carbon black; CNF = carbon nano fiber.

Table S5. Inorganic cathode materials for aqueous zinc-organic batteries have been reported in the literature.

Structure	**Composition of Electrode (active material**: conductive carbon: binder)	**Electrolyte**	**Theoretical Capacity (Electron Transfer)**	**Voltage Window (V)**	**Initial Capacity at Lowest Rate Reported**	**Reversible Capacity at Highest Rate Reported**	**Capacity Retention at Highest Rate**	**Ref.**
δ-MnO_2/graphene superlattice	**7 : 2 : 1** (active : Super P : PVDF)	2 M $ZnSO_4$ + 0.1 M $MnSO_4$	NR	0.8–1.8 V	270 mAh g^{-1} @ 1C	165 mAh g^{-1} @ 5C (after 5000 cycles)	At 5C, retains 165 mAh g^{-1} after >5000 cycles	51
β-MnO_2/3D graphene–CNT hybrid	Cathode mix 7 : 2 : 1 (β-MnO_2/3D-GPE/CNT : Super P : PVDF)	2 M $ZnSO_4$ + x M $MnSO_4$ (best: 0.5 M $MnSO_4$)	NR	GCD 1.0–1.8 V; CV 0.8–1.8 V	521.91 mAh g^{-1} @ 100 mA g^{-1} (0.5 M $MnSO_4$)	109.12 mAh g^{-1} @ 1 A g^{-1}	83.8% retention after >8000 cycles @ 1 A g^{-1}	52

Structure	Composition of Electrode (**active material**: conductive carbon: binder)	Electrolyte	Theoretical Capacity (Electron Transfer)	Voltage Window (V)	Initial Capacity at Lowest Rate Reported	Reversible Capacity at Highest Rate Reported	Capacity Retention at Highest Rate	Ref.
δ-$VOPO_4$	6 : 2 : 2 (active δ-$VOPO_4$: Super P : PTFE), coated on Ti mesh	3 M $Zn(CF_3SO_3)_2$	>300 mAh g^{-1} (fully zincified → $ZnVOPO_4$; redox couples include V^{5+}/V^{4+} and V^{4+}/V^{3+}, i.e., up to ~2 e^- per V)	0.3–1.9 V	94.8 mAh g^{-1} @ 0.1C (1C = 330 mA g^{-1})	53 mAh g^{-1} @ 20C	At 10C: 90.88–90.9 mAh g^{-1} after 1000 cycles	53
$V_2O_5 \cdot nH_2O$–PAA	70 : 20 : 10 ($V2O5 \cdot nH_2O$: Super P : PAA (or PVDF for control); NMP solvent; Ti foil collector; thick electrode uses Ti mesh)	3 M $Zn(CF_3SO_3)_2$	NA	0.2–1.6 V	375.6 mAh g^{-1} @ 0.1 A g^{-1}	141.9 mAh g^{-1} @ 5 A g^{-1}	at 2 A g^{-1}: 84.1% after 2000 cycles	54

Structure	Composition of Electrode (**active material**: conductive carbon: binder)	Electrolyte	Theoretical Capacity (Electron Transfer)	Voltage Window (V)	Initial Capacity at Lowest Rate Reported	Reversible Capacity at Highest Rate Reported	Capacity Retention at Highest Rate	Ref.
CNT@M = CNT composite β-MnO_2	7 : 2 : 1 (active : carbon black : PVDF; NMP; coated on Ti foil; ~1.2 mg cm^{-2})	2 M $ZnSO_4$ + 0.1 M $MnSO_4$	NR	0.8–1.9 V	467 mAh g^{-1} @ 0.1 A g^{-1}	259 mAh g^{-1} @ 3 A g^{-1}	At 3 A g^{-1}: 220 mAh g^{-1} after 2000 cycles, 96.4% retention	55
Amorphous Co-doped MnO_2 nanosheets in-situ grown on porous residual carbon (RC)	7 : 2 : 1 (active : acetylene black : PVDF; coated on Ti foil; loading 0.7–1.2 mg cm^{-2})	2.0 M $ZnSO_4$ + 0.1 M $MnSO_4$	NR	0.8–1.9 V	521.0 mAh g^{-1} @ 0.2 A g^{-1}	141.61 mAh g^{-1} @ 3 A g^{-1} (10,000-cycle)	At 3 A g^{-1}: 94.4% retention after 10,000 cycles	56

Structure	Composition of Electrode (**active material**: conductive carbon: binder)	Electrolyte	Theoretical Capacity (Electron Transfer)	Voltage Window (V)	Initial Capacity at Lowest Rate Reported	Reversible Capacity at Highest Rate Reported	Capacity Retention at Highest Rate	Ref.
Amorphous VOx/NC porous core–shell spheres	70 : 20 : 10 (V2O3/NC : acetylene black : PVDF; NMP; coated on stainless steel mesh; loading ~0.8–1.2 mg cm^{-2})	3.0 M $Zn(CF_3SO_3)_2$	NR	0.3–1.9 V	391 mAh g^{-1} @ 0.1 A g^{-1}	152 mAh g^{-1} @ 5 A g^{-1}	At 5 A g^{-1}: 233 mAh g^{-1} after 1500 cycles	57
0.05Ce–VO/NHVO (Ce-doped $VO_2/NH_4V_4O_{10}$ hybrid; nanosheets	7 : 2 : 1 (active : carbon black : PVDF)	3 M $Zn(CF_3SO_3)_2$, with Ce additive	NR	0.2–1.6 V	524 mAh g^{-1} @ 0.1 A g^{-1}	278 mAh g^{-1} @ 10 A g^{-1}	at 5 A g^{-1}: 331 mAh g^{-1} after 4000 cycles (88% retention)	58

Structure	Composition of Electrode (**active material**: conductive carbon: binder)	Electrolyte	Theoretical Capacity (Electron Transfer)	Voltage Window (V)	Initial Capacity at Lowest Rate Reported	Reversible Capacity at Highest Rate Reported	Capacity Retention at Highest Rate	Ref.
$VO_2/NH_4V_4O_{10}$ composite	70 : 20 : 10 (sample : acetylene black : PVDF; NMP; coated on Ti foil)	3 M $Zn(CF_3SO_3)_2$	NR	0.2–1.6 V	403.8 mAh g^{-1} @ 0.1 A g^{-1}	258.6 mAh g^{-1} @ 10 A g^{-1}	73.1% after 1000 cycles @ 5 A g^{-1}	59
Ile–α-MnO_2	7 : 2 : 1 (Ile–α-MnO_2 : Super P : PVDF; coated on carbon paper; loading 1.3–2 mg cm^{-2})	2 M $ZnSO_4$ + 0.2 M $MnSO_4$	NR	0.8–1.8 V	334.9 mAh g^{-1} @ 0.1 A g^{-1}	153.8 mAh g^{-1} @ 1.0 A g^{-1} (after 2000 cycles)	85% retention after 2000 cycles @ 1.0 A g^{-1}	60

Structure	Composition of Electrode (**active material**: conductive carbon: binder)	Electrolyte	Theoretical Capacity (Electron Transfer)	Voltage Window (V)	Initial Capacity at Lowest Rate Reported	Reversible Capacity at Highest Rate Reported	Capacity Retention at Highest Rate	Ref.
PANI–NixV2O5 (PNV) superlattice nanobelts;	7 : 2 : 1 (active : carbon black : PVDF)	3 M $Zn(CF_3SO_3)_2$	NR	0.3–1.7 V	467 mAh g^{-1} @ 0.1 A g^{-1}	261 mAh g^{-1} @ 5 A g^{-1}	At 5 A g^{-1}: 89.5% retained after 1000 cycles	61
VO2/V2O3/V6O13 @N–C nanosheets	7 : 2 : 1 (active : conductive carbon : PVDF; on stainless-steel mesh)	3 M $Zn(CF_3SO_3)_2$	NR	0.2–1.5 V	288.4 mAh g^{-1} @ 0.1 A g^{-}	198.2 mAh g^{-1} @ 5 A g^{-1}	At 5 A g^{-1}: 86.5% retained after 2000 cycles	62

Structure	Composition of Electrode (**active material**: conductive carbon: binder)	Electrolyte	Theoretical Capacity (Electron Transfer)	Voltage Window (V)	Initial Capacity at Lowest Rate Reported	Reversible Capacity at Highest Rate Reported	Capacity Retention at Highest Rate	Ref.
CoVO multiphase vanadium oxide (CoVO-3)	7 : 2 : 1 (CoVO : acetylene black (Super P) : PVDF), coated on 400-mesh stainless-steel foil	2 M ZnSO4	VO2 theoretical 323 mAh g^{-1}	0.2–1.3 V	317 mAh g^{-1} @ 0.1 A g^{-1}	NA	At 5 A g^{-1}: 89.71% retention after 2000 cycles	63
V2O3/Zn3V3O8@C heterostructure	7 : 2 : 1 (active : acetylene black : PVDF), coated on Ti foil; loading ~1 mg cm^{-2}	3 M $Zn(CF_3SO_3)_2$	V2O3 theoretical 715 mAh g^{-1} (two-electron redox)	0.2–1.6 V	419.0 mAh g^{-1} @ 0.1 A g^{-1}	235.8 mAh g^{-1} @ 2 A g^{-1}	At 2 A g^{-1}: 80.6% retention after 1000 cycles	64

Structure	Composition of Electrode (**active material**: conductive carbon: binder)	Electrolyte	Theoretical Capacity (Electron Transfer)	Voltage Window (V)	Initial Capacity at Lowest Rate Reported	Reversible Capacity at Highest Rate Reported	Capacity Retention at Highest Rate	Ref.
NS-MnO_2 = N,S dual-anion doped layered δ-MnO_2 nanosheets	7 : 2 : 1 (NS-MnO_2 : Super P : PVDF)	2 M $ZnSO_4$ + 0.1 M $MnSO_4$	NR	0.8–1.8 V	304 mAh g^{-1} @ 0.2 A g^{-1}	74 mAh g^{-1} @ 2.0 A g^{-1}	At 2 A g^{-1}: 90 mAh g^{-1} with 90% retention after 2000 cycles	65
KMO/CNFs = K^+-intercalated δ-MnO_2 grown in situ on flexible N-doped carbon nanofiber membrane	KMO/CNFs used directly as cathode; no active:carbon:binder	2 M $ZnSO_4$ / 0.3 M $MnSO_4$	NR	0.7–1.8 V	472 mAh g^{-1} @ 0.3 A g^{-1}	236 mAh g^{-1} @ 3.0 A g^{-1}	At 3 A g^{-1}: 190 mAh g^{-1} after 1000 cycles	66

Structure	Composition of Electrode (**active material**: conductive carbon: binder)	Electrolyte	Theoretical Capacity (Electron Transfer)	Voltage Window (V)	Initial Capacity at Lowest Rate Reported	Reversible Capacity at Highest Rate Reported	Capacity Retention at Highest Rate	Ref.
Flower-like VO2@V2O5 heterojunction	70 : 20 : 10 (active : Super P : PVDF)	3 M Zn(CF3SO3)2	NR	0.2–1.4 V	316.45 mAh g^{-1} @ 50 mA g^{-1}	219.36 mAh g^{-1} @ 1000 mA g^{-1}	At 1000 mA g^{-1}: 95.3% retention after 1200 cycles	67
R-MnO2@Mn-CSN	7 : 2 : 1 (active : Ketjen black : PVDF; coated on stainless-steel foil)	3 M ZnSO4 (Mn2+-free baseline electrolyte)	NR	0.6–1.8 V	278.3 mAh g^{-1} @ 0.1 A g^{-1}	41.04 mAh g^{-1} @ 5 A g^{-1}	At 5 A g^{-1}: 35.14 mAh g^{-1} after 5000 cycles (83.21%)	68

Structure	**Composition of Electrode (active material**: conductive carbon: binder)	**Electrolyte**	**Theoretical Capacity (Electron Transfer)**	**Voltage Window (V)**	**Initial Capacity at Lowest Rate Reported**	**Reversible Capacity at Highest Rate Reported**	**Capacity Retention at Highest Rate**	**Ref.**
Crystalline $MnCO_3$@amorphous MnO_x	70:20:10 (active : acetylene black : PVDF)	2.0 M $ZnSO_4$ + 0.1 M $MnSO_4$	NA	0.8–1.85 V	316.9 mAh g^{-1} @ 0.1 A g^{-1}	99.7 mAh g^{-1} @ 5.0 A g^{-1} (after 2000 cycles)	71.6% after 2000 cycles @ 5.0 A g^{-1}	69
V_2O_3/VN@GO heterojunction	7:2:1 (active : acetylene black : PVDF)	3 M $Zn(CF_3SO_3)_2$	V_2O_3: 715 mAh g^{-1} (two-electron redox)	0.2–1.6 V	488.1 mAh g^{-1} @ 0.5 A g^{-1}	219.3 mAh g^{-1} @ 10 A g^{-1}	91.4% after 3000 cycles @ 10 A g^{-1}	70

Structure	Composition of Electrode (**active material**: conductive carbon: binder)	Electrolyte	Theoretical Capacity (Electron Transfer)	Voltage Window (V)	Initial Capacity at Lowest Rate Reported	Reversible Capacity at Highest Rate Reported	Capacity Retention at Highest Rate	Ref.
$Al_{0.1}$–MnO_2	**$Al_{0.1}$–MnO_2** *in-situ* grown on CC	2 M aqueous $ZnSO_4$+ 0.1 M aqueous $MnSO_4$	N/A	0.8–1.8	328 mAh g^{-1} at 200 mA g^{-1}	201.6 mAh g^{-1} at 1 A g^{-1} (136 mAh g^{-1} at 8 A g^{-1} for 7 cycles)*	87% after 1000 cycles at 1 A g^{-1}	71
Amino PEG amine-Ammonium vanadium oxide nanorods	**APA-NVO_4**:SP:PVDF (8:1:1)	3 M aqueous $Zn(CF_3SO_3)_2$	N/A	0.1–2.0	377 mAh g^{-1} at 100 mA g^{-1}	105 mAh g^{-1} at 3 A g^{-1}	94% after 1200 cycles at 3 A g^{-1} (ED = 680 Wh kg^{-1})	72

Structure	Composition of Electrode (**active material**: conductive carbon: binder)	Electrolyte	Theoretical Capacity (Electron Transfer)	Voltage Window (V)	Initial Capacity at Lowest Rate Reported	Reversible Capacity at Highest Rate Reported	Capacity Retention at Highest Rate	Ref.
Mn-based Prussian blue analogs	**Mn@Fe_1-PBA**:SP:PVDF (6:3:1)	1 M aqueous $ZnSO_4$	N/A	0.0–2.25	195 mAh g^{-1} at 1 A g^{-1}	47 mAh g^{-1} at 5 A g^{-1} (47 mAh g^{-1} at 10 A g^{-1} for 10 cycles)*	71% after 3000 cycles at 5 A g^{-1} (ED = 82 Wh kg^{-1}; PD = 7.82 kW kg^{-1})	73

References

(1) Chen, Y.; Li, J.; Zhu, Q.; Fan, K.; Cao, Y.; Zhang, G.; Zhang, C.; Gao, Y.; Zou, J.; Zhai, T. Two-dimensional organic supramolecule via hydrogen bonding and π–π stacking for ultrahigh capacity and long-life aqueous zinc–organic batteries. *Angew. Chem. Int. Ed.* **2022**, *134*, e202116289.

(2) Buyukcakir, O.; Yuksel, R.; Begar, F.; Erdogmus, M.; Arsakay, M.; Lee, S. H.; Kim, S. O.; Ruoff, R. S. Ultralong-life quinone-based porous organic polymer cathode for high-performance aqueous zinc-ion batteries. *ACS Appl. Energy Mater.* **2023**, *6*, 7672–7680.

(3) Liu, Y.; Li, Z.; Li, C.; Wei, Y.; Yan, S.; Ji, Z.; Zou, S.; Li, H.; Liu, Y.; Chen, C. Imidazole-linked covalent organic polymers with abundant oxygen and nitrogen active centers for advanced aqueous zinc-organic batteries. *Chem. Eng. J.* **2024**, *488*, 150778.

(4) Ma, D.; Zhao, H.; Cao, F.; Zhao, H.; Li, J.; Wang, L.; Liu, K. A carbonyl-rich covalent organic framework as a high-performance cathode material for aqueous rechargeable zinc-ion batteries. *Chem. Sci.* **2022**, *13*, 2385–2390.

(5) Chen, X.; Ma, Y.; Lu, Y.; Zhang, H.; Yang, B.; Liu, Q. A high-performance chemically self-charging aqueous zinc battery using a porous organic polymer cathode. *Chin. Chem. Lett.* **2024**, *35*, 110666.

(6) Zhang, S.; Long, S.; Li, H.; Xu, Q. A high-capacity organic cathode based on active N atoms for aqueous zinc-ion batteries. *Chem. Eng. J.* **2020**, *400*, 125898.

(7) Wang, W.; Kale, V. S.; Cao, Z.; Kandambeth, S.; Zhang, W.; Ming, J.; Parvatkar, P. T.; Abou-Hamad, E.; Shekhah, O.; Cavallo, L. Phenanthroline covalent organic framework electrodes for high-performance zinc-ion supercapattery. *ACS Energy Lett.* **2020**, *5*, 2256–2264.

(8) Khayum, A.; Ghosh, M.; Vijayakumar, V.; Halder, A.; Nurhuda, M.; Kumar, S.; Addicoat, M.; Kurungot, S.; Banerjee, R. Zinc ion interactions in a two-dimensional covalent organic framework based aqueous zinc ion battery. *Chem. Sci.* **2019**, *10*, 8889–8894.

(9) Wang, W.; Kale, V. S.; Cao, Z.; Lei, Y.; Kandambeth, S.; Zou, G.; Zhu, Y.; Abouhamad, E.; Shekhah, O.; Cavallo, L. Molecular engineering of covalent organic framework cathodes for enhanced zinc-ion batteries. *Adv. Mater.* **2021**, *33*, 2103617.

(10) Sun, T.; Li, Z. J.; Zhi, Y. F.; Huang, Y. J.; Fan, H. J.; Zhang, Q. Poly (2, 5-Dihydroxy-1, 4-Benzoquinonyl sulfide) as an efficient cathode for high-performance aqueous zinc–organic batteries. *Adv. Funct. Mater.* **2021**, *31*, 2010049.

(11) Zhang, H.; Xu, D.; Wang, L.; Ye, Z.; Chen, B.; Pei, L.; Wang, Z.; Cao, Z.; Shen, J.; Ye, M. A polymer/graphene composite cathode with active carbonyls and secondary amine moieties for high-performance aqueous Zn-organic batteries involving dual-ion mechanism. *Small* **2021**, *17*, 2100902.

(12) Jiang, B.; Huang, T.; Yang, P.; Xi, X.; Su, Y.; Liu, R.; Wu, D. Solution-processed perylene diimide-ethylene diamine cathodes for aqueous zinc ion batteries. *J. Colloid Interface Sci.* **2021**, *598*, 36–44.
(13) Wang, X.; Wang, G.; He, X. Anthraquinone porous polymers with different linking patterns for high performance zinc-organic battery. *J. Colloid Interface Sci.* **2023**, *629*, 434–444.
(14) Xiang, Y.; Li, X.; Qiu, C.; Yang, W.; Liu, L.; Yu, H.; Zhang, L.; Yan, L.; Shu, J. Proton insertion chemistry in a phenazine-based cathode for aqueous Zn-organic batteries. *Mater. Adv.* **2025**, *6*, 1300–1306.
(15) Zhang, H.; Xie, S.; Cao, Z.; Xu, D.; Wang, L.; Fang, H.; Shen, J.; Ye, M. Extended π-conjugated system in organic cathode with active C═N bonds for driving aqueous zinc-ion batteries. *ACS Appl. Energy Mater.* **2021**, *4*, 655−661.
(16) Li, J.; Huang, L.; Lv, H.; Wang, J.; Wang, G.; Chen, L.; Liu, Y.; Guo, W.; Yu, F.; Gu, T. Novel organic cathode with conjugated N-heteroaromatic structures for high-performance aqueous zinc-ion batteries. *ACS Appl. Mater. Interfaces* **2022**, *14*, 38844–38853.
(17) Shi, Y.; Wang, P.; Gao, H.; Jin, W.; Chen, Y.; Huang, Y.; Wu, T.-R.; Wu, D.-Y.; Xu, J.; Cao, J. π-conjugated N-heterocyclic compound with redox-active quinone and pyrazine moieties as a high-capacity organic cathode for aqueous zinc-ion batteries. *Chem. Eng. J.* **2023**, *461*, 141850.
(18) Wang, Q.; Xu, X.; Yang, G.; Liu, Y.; Yao, X. An organic cathode with tailored working potential for aqueous Zn-ion batteries. *Chem. Commun.* **2020**, *56*, 11859–11862.
(19) Li, S.; Shang, J.; Li, M.; Xu, M.; Zeng, F.; Yin, H.; Tang, Y.; Han, C.; Cheng, H. M. Design and synthesis of a π-conjugated N-heteroaromatic material for aqueous zinc–organic batteries with ultrahigh rate and extremely long life. *Adv. Mater.* **2023**, *35*, 2207115.
(20) Menart, S.; Pirnat, K.; Pahovnik, D.; Dominko, R. Triquinoxalinediol as organic cathode material for rechargeable aqueous zinc-ion batteries. *J. Mater. Chem. A.* **2023**, *11*, 10874–10882.
(21) Menart, S.; Pirnat, K.; Krajnc, A.; Ruiz-Zepeda, F.; Pahovnik, D.; Santa, J. F. V.; Dominko, R. Synthesis of organic cathode materials with pyrazine and catechol motifs for rechargeable lithium and zinc batteries. *J. Power Sources* **2024**, *596*, 234033.
(22) Wang, Y.; Wang, X.; Tang, J.; Tang, W. A Quinoxalinophenazinedione covalent triazine framework for boosted high-performance aqueous zinc-ion batteries. *J. Mater. Chem. A* **2022**, *10*, 13868–13875.
(23) Shi, Y.; Xu, Z.; Wang, P.; Gao, H.; He, W.; Sun, Y.; Huang, Y.; Xu, J.; Cao, J. Tuning the number of redox groups in the cathode toward high rate and long lifespan zinc-ion batteries. *Chem. Commun.* **2024**, *60*, 420–423.

(24) Menart, S.; Luzanin, O.; Pirnat, K.; Pahovnik, D.; Moškon, J. e.; Dominko, R. Design of organic cathode material based on quinone and pyrazine motifs for rechargeable lithium and zinc Batteries. *ACS Appl. Mater. Interfaces* **2024**, *16*, 16029–16039.
(25) Li, W.; Xu, H.; Zhang, H.; Wei, F.; Huang, L.; Ke, S.; Fu, J.; Jing, C.; Cheng, J.; Liu, S. Tuning electron delocalization of hydrogen-bonded organic framework cathode for high-performance zinc-organic batteries. *Nat. Commun.* **2023**, *14*, 5235.
(26) Nam, K. W.; Kim, H.; Beldjoudi, Y.; Kwon, T.-w.; Kim, D. J.; Stoddart, J. F. Redox-active phenanthrenequinone triangles in aqueous rechargeable zinc batteries. *J. Am. Chem. Soc.* **2020**, *142*, 2541–2548.
(27) Na, M.; Oh, Y.; Byon, H. R. Effects of Zn^{2+} and H^{+} association with naphthalene diimide electrodes for aqueous Zn-ion batteries. *Chem. Mater.* **2020**, *32*, 6990–6997.
(28) Zhang, S.; Zhao, W.; Li, H.; Xu, Q. Cross-conjugated polycatechol organic cathode for aqueous zinc-ion storage. *ChemSusChem* **2020**, *13*, 188–195.
(29) Gao, Y.; Li, G.; Wang, F.; Chu, J.; Yu, P.; Wang, B.; Zhan, H.; Song, Z. A high-performance aqueous rechargeable zinc battery based on organic cathode integrating quinone and pyrazine. *Energy Storage Mater.* **2021**, *40*, 31–40.
(30) Chen, Y.; Dai, H.; Fan, K.; Zhang, G.; Tang, M.; Gao, Y.; Zhang, C.; Guan, L.; Mao, M.; Liu, H. A recyclable and scalable high-capacity organic battery. *Angew. Chem. Int. Ed.* **2023**, *135*, e202302539.
(31) Li, C.; Hu, L.; Ren, X.; Lin, L.; Zhan, C.; Weng, Q.; Sun, X.; Yu, X. Asymmetric charge distribution of active centers in small molecule quinone cathode boosts high-energy and high-rate aqueous zinc-organic batteries. *Adv. Funct. Mater.* **2024**, *34*, 2313241.
(32) Wang, Y.; Wang, C.; Ni, Z.; Gu, Y.; Wang, B.; Guo, Z.; Wang, Z.; Bin, D.; Ma, J.; Wang, Y. Binding zinc ions by carboxyl groups from adjacent molecules toward long-life aqueous zinc–organic batteries. *Adv. Mater.* **2020**, *32*, 2000338.
(33) Du, D.; Zhou, J.; Yin, Z.; Feng, G.; Ji, W.; Huang, H.; Pang, S. High-voltage recyclable organic cathode enabled by heteroatomic substitution for aqueous zinc-ion batteries. *Adv. Energy Mater.* **2024**, *14*, 2400580.
(34) Xia, Y.; Wang, X.; Zhou, J. N-Methylpyrrolidone assisted tetrachlorobenzoquinone intercalating V_2O_5 as cathode for aqueous zinc-ion battery. *Chem. Commun.* **2023**, *59*, 6199–6202.
(35) Zhao, Q.; Huang, W.; Luo, Z.; Liu, L.; Lu, Y.; Li, Y.; Li, L.; Hu, J.; Ma, H.; Chen, J. High-capacity aqueous zinc batteries using sustainable quinone electrodes. *Sci. Adv.* **2018**, *4*, eaao1761.
(36) Tie, Z.; Liu, L.; Deng, S.; Zhao, D.; Niu, Z. Proton insertion chemistry of a zinc–organic battery. *Angew. Chem. Int. Ed.* **2020**, *132*, 4920–4924.

(37) Lin, L.; Lin, Z.; Zhu, J.; Wang, K.; Wu, W.; Qiu, T.; Sun, X. A semi-conductive organic cathode material enabled by extended conjugation for rechargeable aqueous zinc batteries. *Energy Environ. Sci.* **2023**, *16*, 89–96.
(38) Wang, Q.; Liu, Y.; Wang, C.; Xu, X.; Zhao, W.; Li, Y.; Dong, H. Vat orange 7 as an organic electrode with ultrafast hydronium-ion storage and super-long life for rechargeable aqueous zinc batteries. *Chem. Eng. J.* **2023**, *451*, 138776.
(39) Niu, S.; Wang, Y.; Zhang, J.; Wang, Y.; Tian, Y.; Ju, N.; Wang, H.; Zhao, S.; Zhang, X.; Zhang, W. Engineering low-cost organic cathode for aqueous rechargeable battery and demonstrating the proton intercalation mechanism for pyrazine energy storage unit. *Small* **2023**, 2309022.
(40) Lin, Z.; Shi, H.-Y.; Lin, L.; Yang, X.; Wu, W.; Sun, X. A high capacity small molecule quinone cathode for rechargeable aqueous zinc-organic batteries. *Nat. Commun.* **2021**, *12*, 4424.
(41) Xu, D.; Cao, Z.; Ye, Z.; Zhang, H.; Wang, L.; John, M.; Dong, P.; Gao, S.; Shen, J.; Ye, M. Electrochemical oxidation of π-π coupling organic cathode for enhanced zinc ion storage. *Chem. Eng. J.* **2021**, *417*, 129245.
(42) Zhang, H.; Zhong, L.; Xie, J.; Yang, F.; Liu, X.; Lu, X. A COF-like N-rich conjugated microporous polytriphenylamine cathode with pseudocapacitive anion storage behavior for high-energy aqueous zinc dual-ion batteries. *Adv. Mater.* **2021***, 33*, e2101857.
(43) Khayum, A.; Ghosh, M.; Vijayakumar, V.; Halder, A.; Nurhuda, M.; Kumar, S.; Addicoat, M.; Kurungot, S.; Banerjee, R. Zinc ion interactions in a two-dimensional covalent organic framework based aqueous zinc ion battery. *Chem. Sci.* **2019***, 10,* 8889–8894.
(44) Wang, W.; Kale, V. S.; Cao, Z.; Kandambeth, S.; Zhang, W.; Ming, J.; Parvatkar, P. T.; Abou-Hamad, E.; Shekhah, O.; Cavallo, L. Phenanthroline covalent organic framework electrodes for high-performance zinc-ion supercapattery. *ACS Energy Lett.* **2020**, *5*, 2256–2264.
(45) Ye, F.; Liu, Q.; Dong, H.; Guan, K.; Chen, Z.; Ju, N.; Hu, L. Organic zinc-ion battery: planar, pi-conjugated quinone-based polymer endows ultrafast ion diffusion kinetics. *Angew. Chem. Int. Ed.* **2022**, *61*, e202214244.
(46) Wang, X.; Tang, J.; Tang, W. Manipulating polymer configuration to accelerate cation intercalation kinetics for high-performance aqueous zinc-ion batteries. *Adv. Funct. Mater.* **2022**, *32*, 2200517.
(47) Peng, H.; Huang, S.; Montes-Garcia, V.; Pakulski, D.; Guo, H.; Richard, F.; Zhuang, X.; Samori, P.; Ciesielski, A. Supramolecular engineering of cathode materials for aqueous zinc-ion energy storage devices: novel benzothiadiazole functionalized two-dimensional olefin-linked COFs. *Angew. Chem. Int. Ed.* **2023**, *62*, e202216136.
(48) Liang, Y.; Xia, Y.; Wang, X.; Zhou, J. An imine-rich polymer with enlarged pi-conjugated planes for aqueous zinc-ion batteries. *Chem. Commun.* **2023**, *59*, 12927–12930.

(49) Zhang, C.; Ma, W.; Han, C.; Luo, L.-W.; Daniyar, A.; Xiang, S.; Wu, X.; Ji, X.; Jiang, J.-X. Tailoring the linking patterns of polypyrene cathodes for high-performance aqueous Zn dual-ion batteries. *Energy Environ. Sci.* **2021**, *14*, 462–472.

(50) Wang, X.; Xiao, J.; Tang, W. Hydroquinone versus pyrocatechol pendants twisted conjugated polymer cathodes for high-performance and robust aqueous zinc-ion batteries. *Adv. Funct. Mater.* **2022**, *32*, 2108225.

(51) Wang, S., Guo, X., Huang, K., Achari, A., Safaei, J., Lei, Y., Li, D., Gu, Q., Sun, C., Gloag, L., Langford, S., Geim, A., Nair, RR., & Wang, G. Cooperative Jahn-Teller effect and engineered long-range strain in manganese oxide/graphene superlattice for aqueous zinc-ion batteries. Nat. Commun. 16 (2025) 5191.

(52) Jin, D., Dong, X., Xin, S., Yang, L., Liu, J., & Pang, Q. Effect of MnSO4 concentration on the electrochemical performance of β-MnO2/3D graphene-carbon nanotube hybrids cathode for aqueous zinc-ion batteries. Ionics. 30 (2024) 3329-3338.

(53) Zhao, D., Pu, X., Tang, S., Ding, M., Zeng, Y., Cao, Y., & Chen, Z. δ-VOPO 4 as a high-voltage cathode material for aqueous zinc-ion batteries. Chem. Sci. 14 (2023) 8206-8213.

(54) Liu, H., Sun, J., Sun, P., Zhao, C., Ma, T., Shi, X., Wang, Y., & Wei, Y. Polyacrylic Acid Binder Enabling High Areal Capacity V2O5· nH2O Cathode for Aqueous Zinc-Ion Batteries. Small, 21 (2025), 2503069.

(55) Li, L., Yin, C., Han, R., Zhong, F., & Hu, J. CNT composite β-MnO2 with fiber cable shape as cathode materials for aqueous zinc-ion batteries. Inorg. Chem. 63 (2024), 13100-13109.

(56) Li, Z., Wu, C., & Yin, C. Residual carbon induced amorphous MnO2 as a long-life cathode for aqueous zinc ion batteries. Electrochim. Acta. 542, (2025) 147537.

(57) Yuan, J., Gan, Y., Mou, J., Ma, X., Li, X., Meng, J., Xu, L., Zhang, X., He, H., & Liu, J. Electrochemically induced amorphous and porous VO x/N-doped carbon spheres as a cathode for advanced aqueous zinc-ion batteries." Inorg. Chem. Front. 10 (2023) 984-990.

(58) Zhao, M., Wu, X., & Bando, Y. Structural optimization of VO 2/NH 4 V 4 O 10 cathode materials for high-performance wide-temperature zinc-ion batteries. Inorg. Chem.Front. 12 (2025) 7123-7132.

(59) Chen, L., Zheng, Y., Zhang, Z., Ma, Y., Wang, Y., Xiao, H., Xu, M., Li, Z., & Yuan, G. Optimizing ammonium vanadate crystal structure by facile in situ phase transformation of VO 2/NH 4 V 4 O 10 with special micro–nano feature for advanced aqueous zinc ion batteries. Inorg. Chem. Front. 11 (2024) 1266-1278.

(60) Ding, Y., Cai, C., Ma, L., Wang, J., Mercer, MP, Liu, J., Kramer, D., Yu, X., Xue, D., Zhi, C., & Peng, C. Tailoring MnO2 Cathode Interface via Organic–Inorganic Hybridization Engineering for Ultra-Stable Aqueous Zinc-Ion Batteries. Adv. Energy Mater. 15 (2025), 2402819.
(61) Mao, S., Wu, Y., Xu, S., Xiao, T., Li, Y., Li, Z., Pan, X., Yuan, B., Xu, Y., Wen, H., Sui, Q., Quan, Y., & Liu, J. Design of large-spacing, high-stability PANI-NixV2O5 nanobelts as cathode for aqueous zinc-ion batteries using an organic-inorganic co-embedding strategy. J. Power Sources. 628 (2025) 235912.
(62) Li, Y., Yao, Z., Wang, C., Wang, K., Gu, D., Wang, L., Zou, Y., & *Ren*, X., Multiple heterostructures, rich oxygen vacancies and expansion counteraction effect co-boosted VO 2/V 2 O 3/V 6 O 13@ nitrogen-doped carbon nanosheets as a high-performance cathode for aqueous zinc-ion batteries." Dalton Trans. 54 (2025), 7004-7013.
(63) Zhai, X., Li, R., Zhang, Z., Wang, X., Zhang, L., Shang, C., Zhang, H., Zhao, C., & Liu, D. Cobalt-ion-doped vanadium-based cathodes with multiphase coexistence for high-performance aqueous zinc-ion batteries. Inorg. Chem. Commun, 185 (2025) 116085.
(64) Yang, YY, Wang, M., Zhang, Q., Wang, RH, Zheng, Q., Zhang, R., Lin, D., & Huo, Y. Heterostructures Coupling with Oxygen Vacancies Enable High Performance V2O3/Zn3V3O8@ C Cathode for Aqueous Zinc-Ion Batteries. Small. 22 (2025) e09861.
(65) Liang, J., Zhao, Y., Ren, L., Li, M., Zhang, Q., Wang, Y., Sun, X., Chuai, M., Wang, X., & Liu, W. Dual anions doping enhanced conductivity and stability of layered δ-MnO2 cathode for aqueous zinc-ion battery. Adv. Func. Mater. 35 (2025) 2501135.
(66) Yang, J., Yao, G., Li, Z., Zhang, Y., Wei, L., Niu, H., Chen, Q., & Zheng, F. Highly flexible K-intercalated MnO2/carbon membrane for high-performance aqueous zinc-ion battery cathode. Small, 19 (2023), 2205544.
(67) Zhu, H., Jiang, J., Liu, X., Dai, W., Huang, J., Wu, J., & Shi, W. Novel flower like VO2@ V2O5 cathode for boosting high performance aqueous zinc ion batteries. Inorg. Chem. Commun. 170 (2024) 113195.
(68) Ho, S., Tan, Y., Chen, Z., Lin, K., Zhou, C., Liu, P., Huang, S., & Yang, Y. A A Mn coordination supramolecular network inhibits the dissolution of R-MnO2 cathode for ultra-long-cycling zinc-ion battery. Inorg. Chem. Commun. 180 (2025) 115105.
(69) Chen, T., Zhao, S., Liu, Y., Li, G., Cui, Y., Qiu, J., Lian, J., & Zhang, B. Crystalline MnCO3@ Amorphous MnO x Composite as Cathode Material for High-Performance Aqueous Zinc-Ion Batteries. Inorg. Chem. 63 (2024) 9864-9876.
(70) Gong, F., Di, WF, Ding, YJ, Chen, SY, Zhou, YX, Zhang, R., Lin D., & Huo, Y. Construction of V 2 O 3/VN@ GO heterojunction cathodes derived from polyoxovanadates for high-performance aqueous zinc ion batteries. Inorg. Chem. Front. 12 (2025), 4459-4469.
(71) Zhao, Y.; Zhang, S.; Zhang, Y.; Liang, J.; Ren, L.; Fan, H. J.; Liu, W.; Sun, X. Vacancy-rich Al-doped MnO_2 cathodes break the trade-off between kinetics and stability for high-performance aqueous Zn-ion batteries. *Energy Environ. Sci.* **2024**, *17*, 1279–1290.

(72) Zafar, S.; Sharma, M.; Mahapatra, S. N.; Lochab, B. An aqueous zinc-ion battery with an organic–inorganic nanohybrid cathode featuring high operating voltage and long-term stability. *Chem. Commun.* **2025**, *61*, 3151–3154.
(73) Fu, H.; Wang, X.; Ye, L.; Wu, Z.; Yang, J.; Shi, M.; Ang, E. H. Optimizing Fe in Mn-based Prussian blue analogs with dual redox-active sites to enhance operating voltage and durability in Zn-ion batteries. *Chem. Eng. J.* **2025**, *506*, 160308.